

Finite-size-effect-induced topological phase transition in a topological crystalline insulator

Hideyuki Ozawa, Ai Yamakage, Masatoshi Sato, and Yukio Tanaka
Department of Applied Physics, Nagoya University, Nagoya 464-8603, Japan
 (Dated: June 22, 2021)

We study electronic states and topological invariants of (001)-films of topological crystalline insulator (TCI) $\text{Pb}_x\text{Sn}_{1-x}\text{Te}$. Gapless surface Dirac cones on bulk TCIs become gapped in thin films due to finite-size effect, which is hybridization between those on the top and bottom surfaces. We clarify that the TCI film has the strong finite-size effect as compared to three-dimensional topological insulators such as Bi_2Se_3 . Moreover, the energy gap oscillates with the thickness of film. The oscillation stems from topological phase transitions in two dimensions. The obtained data of the topological invariants and energy gap serve as guide to TCI-device applications.

PACS numbers: 71.20.-b, 73.20.At, 71.70.Ej

I. INTRODUCTION

Topological insulators (TIs) are a new state of matter which supports Dirac fermions on its surface and exhibit novel phenomena resulting from the Dirac fermions.¹⁻³ A prototypical TI is quantum Hall insulator in which time-reversal symmetry is broken. In recent years, on the other hand, time-reversal symmetric TI has attracted much attention. Interestingly, symmetry, e.g., time-reversal, gives rise to nontrivial topological number and related topological phenomena. Various symmetries in condensed matters are expected to yield diverse topological materials.

Surface Dirac fermions on TIs are protected by time-reversal symmetry. Nowadays, so-called topological crystalline insulators (TCIs),⁴ which are a nontrivial insulator supporting surface Dirac fermions protected by crystal symmetry, has been proposed⁵ and experimentally discovered⁶⁻⁸ in IV-VI semiconductors. Topological protection by crystalline symmetry enables us to find new topological systems even in insulators which have been thought to be topologically trivial. Moreover, the mechanism different from that of TI can lead to different topological phenomena. Indeed, many materials⁹⁻¹³ and theoretical studies¹⁴⁻²⁴ on TCI have been reported. Furthermore, superconductivity²⁵ and its topological non-triviality²⁶ in a doped TCI has been observed and attracted attentions.²⁷⁻³³

TCIs are not so robust since the crystal symmetry can be easily broken by an external field. Nonetheless, this behavior can be applied to a highly controllable device: an external electric field breaking the crystal symmetry may control the gap of the surface Dirac fermions. Note that this is a great advantage for device application. TI device, in principle, can be realized but needs a magnetic field, which is not convenient in a nano-sized system, to open and control energy gap in the surface Dirac fermions. An electric field is, on the other hand, easily implemented in devices, such as field-effect transistor.

From the perspective of topological material design and its application, nano-fabrication, e.g., thin film and

heterostructure, is one of the most promising ways: the number of carriers in thin films can be highly controlled by applying gate voltage, and electronic states and its dimensionality can be dramatically tuned in heterostructures. Indeed, there are many studies on thin films³⁴⁻⁴⁵ and heterostructures⁴⁶⁻⁵¹ of TIs. Furthermore, several studies on nano-fabrication of TCIs have been reported; field-effect devices with using TCI,⁵²⁻⁵⁴ TCI heterostructure,⁵⁵ and experimental fabrication of TCI films.⁵⁶⁻⁵⁸ Now device application of TCIs is becoming active.

In this paper, we study electronic states and topological invariants of thin film of $\text{Pb}_x\text{Sn}_{1-x}\text{Te}$. In the thin film, the surface Dirac cones become gapped since the wave functions of the top and bottom surface states hybridize with each other. As the number of layers N_z increases, the induced gap decays exponentially but slowly as compared to TIs such as Bi_2Se_3 . For the odd numbers of layers, we find that the energy gap shows a damped oscillation as a function of N_z , which stems from two types of topological phase transition in two dimensions: one is that between a trivial to two-dimensional TCIs, and the other is that between two TCIs. The former transition is in agreement with that obtained in Ref. 53. And also, a similar damped oscillation of the energy gap is found in the even numbers of layers, which accompanies another topological phase transition. These non-monotonic change of the energy gap and topological phase are qualitatively and quantitatively clarified. Our results are useful for experiments on thin films of TCIs.

The paper is organized as follows. In Sec. II, we present electronic states of a (001)-film of $\text{Pb}_x\text{Sn}_{1-x}\text{Te}$. Thickness dependence of the energy gap is closely shown. The causes of this dependence are resolved in terms of topological invariants in Sec. III. Gapless edge states related to the topological invariants are also clarified. Finally we summarize our results in Sec. IV. The details of the model Hamiltonian, symmetry, and the topological numbers are explained in Appendices.

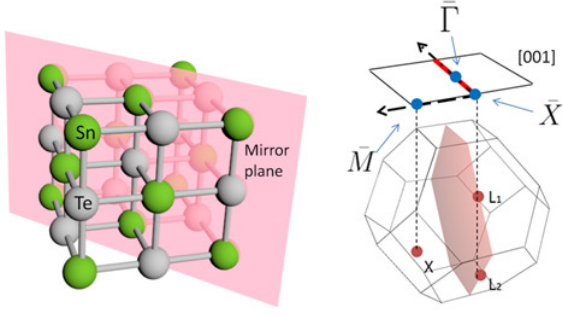


FIG. 1. Crystal structure of SnTe, the first Brillouin zone, and its projection onto the (001) plane. Mirror symmetry with respect to (110) plane illustrated in the figure protects the surface Dirac cones.

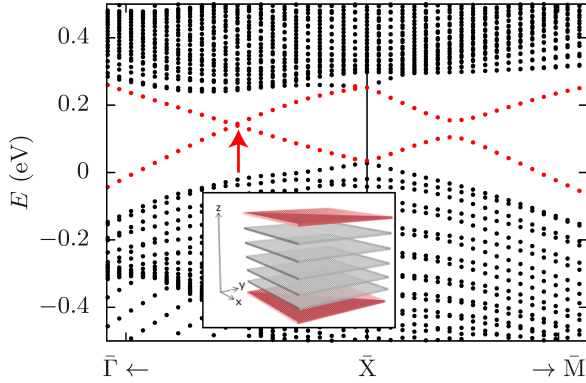


FIG. 2. Energy dispersion for SnTe near the \bar{X} point in slab geometry shown in the inset. The arrow denotes the Dirac point of the surface states. The number of layers is set to $N_z = 45$. The parameters for SnTe are taken from Ref. 59.

II. ENERGY GAP INDUCED BY FINITE-SIZE EFFECT

Bulk $\text{Pb}_x\text{Sn}_{1-x}\text{Te}$ is a TCI, which supports gapless Dirac cones protected by the (110)-reflection symmetry. Firstly, we review the gapless surface states on the bulk system. Next, we show extensive data on the energy gap induced by the finite-size effect in thin films of $\text{Pb}_x\text{Sn}_{1-x}\text{Te}$.

A. Gapless surface states on the bulk

We use a model Hamiltonian of IV-VI semiconductors with s , p , and d orbitals.⁵⁹ The fcc crystal structure and the corresponding first Brillouin zone are illustrated in Fig. 1. The bottom of conduction band and top of valence band are located near the L points. The L points are projected onto the \bar{X} points on the (001) surface. Figure 2 shows an energy dispersion for a thick SnTe slab, where two surface Dirac cones are located on the

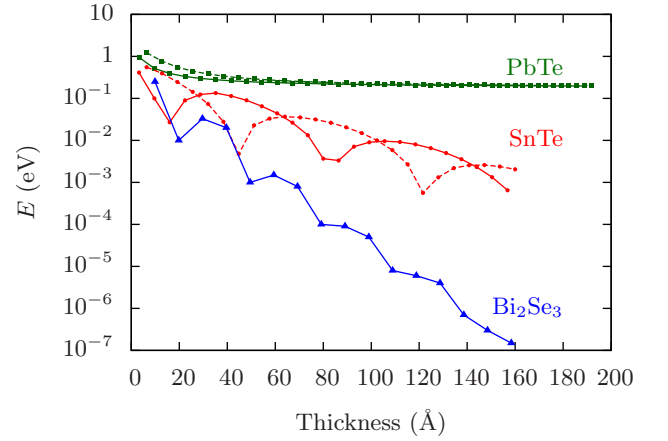


FIG. 3. Finite-size-effect-induced energy gap for thin films of non-topological PbTe [(green) square], TCI SnTe [(red) circle], and TI Bi_2Se_3 [(blue) triangle] as a function of the thickness. The solid and dashed lines denote the magnitude of energy gap for the odd and even numbers of layers, respectively.

$\bar{\Gamma}\bar{X}$ line. The model of IV-VI semiconductor with the (001) surface is explicitly shown in Appendix A 1. The Dirac cones are protected by the mirror Chern number in the (110) surface.⁵ On the contrary, there is no gapless surface states along the $\bar{X}\bar{M}$ nor $\bar{\Gamma}\bar{M}$ lines. Note that in this model the origin of energy is set to the top of valence bands, and the Fermi energy is located at the Dirac point ($E \sim 0.15\text{eV}$) for charge neutral cases.

B. Strong finite-size effect in SnTe

Next we turn to energy gap in the (001) thin film. A wave function of the gapless surface states decays exponentially into the bulk $\psi \sim e^{-z/\xi}$ with the penetration depth ξ . For the thin film case, the tails of wave functions of the surface states localized on the top and bottom surfaces overlap with each other. In consequence, energy gap ($\sim e^{-N_z/\xi}$) of the surface states is induced due to the finite-size effect. The induced gap for TCI SnTe film are shown in Fig. 3. The induced gap for TI Bi_2Se_3 film (see Appendix A 3), and energy gap for a trivial insulator PbTe film are also shown as a reference. The energy gap of PbTe film is nearly independent of the thickness, and reaches to be 0.2eV which is the magnitude of the bulk gap, since PbTe has no gapless surface state. On the other hand, the energy gap of SnTe film decreases exponentially ($\xi \sim 10 \text{ layers} \sim 30 \text{ Å}$) and oscillates as the thickness increases. We firstly focus on the damping part. The oscillation part will be discussed in the next section. In the thick limit, the energy gap of SnTe vanishes and gapless surface Dirac cones are reproduced on the (001) surface. As a reference, the energy gap of Bi_2Se_3 film is shown. The energy gap decreases and oscillates more quickly ($\xi \sim 1 \text{ quintuple layer} \sim 10 \text{ Å}$) than that of SnTe

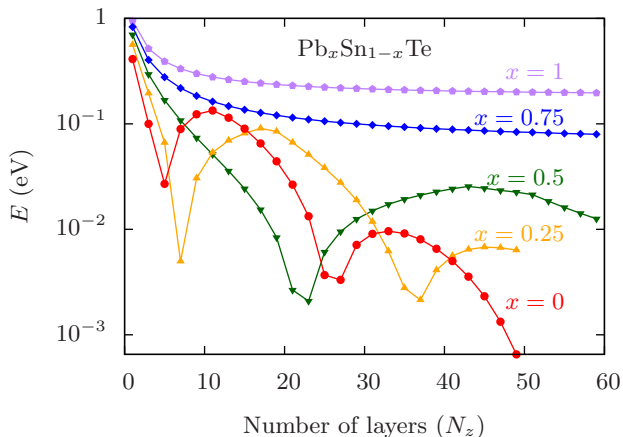


FIG. 4. Energy gap in thin film of $\text{Pb}_x\text{Sn}_{1-x}\text{Te}$ for various compositions x for the odd numbers of layers.

film. The difference comes from crystal structure: SnTe is a cubic crystal, and Bi_2Se_3 is a rhombohedral crystal with quintuple layered structure. Namely, in SnTe , all the bondings are equivalent. But in Bi_2Se_3 , the bonding between the quintuple layers is weak. This is the reason why the finite-size effect in (001) thin film of SnTe is much stronger than that of Bi_2Se_3 .

We quantitatively clarify the magnitude of the finite-size-effect induced gap in $\text{Pb}_x\text{Sn}_{1-x}\text{Te}$ thin films (Fig. 4). For $x \geq 0.75$, the system is in the trivial phase. As the thickness increases, the energy gap decreases exponentially and converges to be the bulk band gap (0.2eV for PbTe and 0.08eV for $\text{Pb}_{0.75}\text{Sn}_{0.25}\text{Te}$) in the thick limit. At $0.5 < x < 0.75$, the topological phase transition occurs and the system falls into the TCI phase in $x \leq 0.5$. In the TCI phase, the energy gap decays as $\sim e^{-N_z/\xi}$. As can be seen from Fig. 4, the decay ratio of the energy gap ($\sim \xi^{-1}$) is proportional to the *distance* from the topological phase transition point. Just at the transition point ($0.5 < x < 0.75$), the energy gap decays extremely slowly ($\xi \rightarrow \infty$).

C. Oscillation of the energy gap

The calculated results shown in Figs. 3 and 4 exhibit oscillation of the energy gap for the TCI films in addition to the exponential decay as a function of the thickness. Such a damped oscillation is known to exist in TI Bi_2Se_3 .^{34–41} Moreover, an even-odd effect also appears in the energy gap (see SnTe in Fig. 3). This behavior is understood intuitively as follows: the top and bottom layers are the same (different) for odd (even) numbers of layers of the (001) film. Actually, the even and odd numbers of layers have different symmetries and are characterized by different topological invariants, as we shall see in Sec. III.

Here we show the details on the oscillation for odd numbers of layers of $\text{Pb}_x\text{Sn}_{1-x}\text{Te}$ (Fig. 4). In the triv-

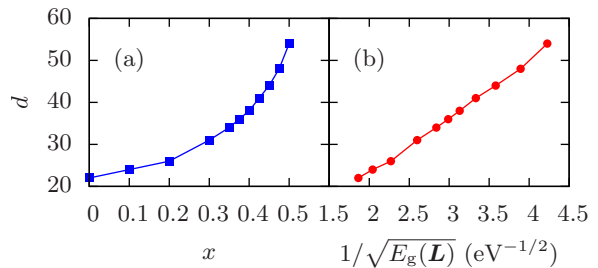


FIG. 5. Period d of oscillation of the energy gap in the film in unit of the number of layers as a function of x (a) and of $1/\sqrt{E_g(\mathbf{L})}$ (b) with $E_g(\mathbf{L})$ the bulk band gap at the L point.

ial phase ($x \geq 0.75$) the energy gap does not oscillate. At the topological phase transition point (located at $0.5 < x < 0.75$), the energy gap closes in $N_z \rightarrow \infty$, i.e., the period of the oscillation is regarded to be infinity. Apart from the transition point, $x \leq 0.5$, the period becomes shorter, and takes to be about 20 layers for $x = 0$. On the other hand, the period of the oscillation in Bi_2Se_3 is about three quintuple-layers, which is one order of magnitude shorter than that of SnTe . Namely, in materials with the strong finite-size effect, the magnitude of the energy gap slowly decays and oscillates with a long period as a function of the thickness. Note that the period in TI films is given by $\pi\sqrt{B/M_0}$,³⁶ where M_0 and B correspond to the magnitude of bulk band gap and effective mass, respectively (see Appendix A 3). We find an empirical rule for the period in a $\text{Pb}_x\text{Sn}_{1-x}\text{Te}$ film, which is similar to that for TI films. The period is scaled by $\sqrt{1/E_g(\mathbf{L})}$ with $E_g(\mathbf{L})$ the magnitude of band gap at the L point in the bulk, as shown in Fig. 5.

D. Discussion

To summarize the finite-size-effect-induced energy gap of TCI films, a damped oscillation occurs in the energy gap as a function of the thickness, whose period is about 20 layers ($\sim 60\text{\AA}$). A TCI film has an advantage over the bulk system: bipolar transport can be realized with applying a gate voltage. The Fermi level can be tuned also to the Dirac point on the surface states of the bulk TCI. Our result shows the penetration depth of wave function of the surface states in the film is about 10 layers ($\sim 30\text{\AA}$). In order to use $\text{Pb}_x\text{Sn}_{1-x}\text{Te}$ film as a three-dimensional TCI, the number of layers must be set to $N_z \gg 10$. Alternatively, it is useful that the thickness is set to the *hot spot* (for SnTe , $N_z \sim 20\text{\AA}$, 40\AA , 80\AA , 120\AA , \dots , see Fig. 3) which is a minimal value in the damped oscillation.

With decreasing the thickness, the system crossovers from three-dimensional to two-dimensional insulators around $N_z \sim \xi \sim 10$, energy gap of the surface states becomes larger. The crossover is schematically summarized in Fig. 6. In exchange for gapless surface states,

the thin film works as a two-dimensional TCI with one-dimensional edge states, which will be explained in the next session.

III. TOPOLOGICAL PHASE DIAGRAM

In this section, we show that oscillatory behavior of the energy gap found in the previous section stems from topological phase transitions, i.e., the energy gap takes a minimal value in the vicinity of the transition point. The corresponding gapless edge states are also discussed. The film has the (001)-reflection symmetry defined by $\mathcal{M}H(k_x, k_y)\mathcal{M}^\dagger = H(k_x, k_y)$ with

$$\mathcal{M}c_n(k_x, k_y)\mathcal{M}^\dagger = \eta M c_{N_z+1-n}(k_x, k_y), \quad M = -iP_z s_z, \quad (1)$$

where H is Hamiltonian of the film, P_z is the (001)-reflection operator acting on the orbitals, s_z is the z -component of spin, c_n is the annihilation operator in the n -th layer for $n = 1, \dots, N_z$, and η is a phase factor as $\eta = -1$ for $N_z = 4m - 3$, $N_z = 4m - 2$, and $\eta = +1$ for $N_z = 4m - 1$, $N_z = 4m$ with $m \in \mathbb{N}$. Since the (001)-reflection symmetry is preserved in the odd numbers of layers,⁵³ one can define the mirror Chern number. Additionally, the (001)-reflection symmetry can be extended to the even numbers of layers, as explained in Appendix B. As a result, the Hamiltonian of the even and odd numbers of layers is decomposed into the mirror-even H_+ and mirror-odd H_- sectors, which has the definite mirror eigenvalue of $M = +i$ (mirror-even) and $M = -i$ (mirror-odd), as

$$\begin{aligned} H(k_x, k_y) &= H_+(k_x, k_y) \oplus H_-(k_x, k_y), \\ H_\pm(k_x, k_y) &= P_\pm H(k_x, k_y) P_\pm, \end{aligned} \quad (2)$$

with the projection operator P_\pm onto the mirror-even/odd sector

$$P_\pm = \sum_m |\pm, m\rangle \langle \pm, m|, \quad \mathcal{M}|\pm, m\rangle = \pm i|\pm, m\rangle, \quad (4)$$

with $|\pm, m\rangle$ being the m -th eigenvector of \mathcal{M} with an eigenvalue of $\pm i$.

Differently from the odd numbers of layers, since time-reversal symmetry is preserved in each mirror sector for the even numbers of layers (see Appendix B 3), the mirror Chern number vanishes. Instead, we introduce a topological invariant characterizing bulk energy bands and gap in the even numbers of layers. The results for the even and odd numbers of layers are summarized in Fig. 6. The details are explained in the following sections.

A. Odd numbers of layers

1. Phase diagram

The topological phase of the odd numbers of layers is characterized by the (001)-mirror Chern number N_M ,⁵³

which is defined by

$$N_M = \frac{N_+ - N_-}{2}, \quad (5)$$

where N_+ and N_- denote the Chern number for the mirror-even and mirror-odd sectors, respectively. N_\pm is calculated by the method proposed in Ref. 60. The obtained topological phase diagram for the odd numbers of layers is shown in Fig. 7 with the magnitude of the energy gap. For the odd numbers of layers of SnTe film with $N_z \leq 3$ and $N_z \geq 5$, the mirror Chern number N_M is obtained to be $N_M = 0$ and $|N_M| = 2$, respectively. The topological phase transition occurs between $N_z = 3$ and $N_z = 5$. At this time the band gap closes at the \bar{X} point.⁵³ This is why the energy gap takes a minimal value between $N_z = 3$ and $N_z = 5$. The same tendency is seen for $x = 0.25$ and $x = 0.5$: the topological phase transition from trivial to $|N_M| = 2$ insulators occurs at $7 < N_z < 9$ for $x = 0.25$ and at $21 < N_z < 23$ for $x = 0.5$. On the other hand, for $x \geq 0.75$, there exists no non-trivial phase for any N_z .

2. Edge state

Next we investigate detail electronic states of the (100)-edge states. The one-dimensional projected Brillouin zone onto the (100) edge is defined in $k_y \in [-\pi, \pi]$ as illustrated in Fig. 6(d). Edge spectral function $\rho_\pm(k_y, E)$ in each mirror sector is defined by

$$\rho_\pm(k_y, E) = \text{Im} \lim_{N_x \rightarrow \infty} \frac{1}{E - \tilde{H}_\pm(k_y) + i0} \Big|_{n_x = N_x}, \quad (6)$$

in the semi-infinite system,⁶¹ where $\tilde{H}_\pm(k_y) = P_\pm \tilde{H}(k_y) P_\pm$ is the Hamiltonian in each mirror sector and $\tilde{H}(k_y)$ is a Hamiltonian of the film with (100) defined in Appendix A 2. The edge charge $\rho_{\pm,c}(k_y, E)$ and spin $\rho_{\pm,s}(k_y, E)$ spectral functions for the mirror-even and mirror-odd sectors are defined by

$$\rho_{\pm,c}(k_y, E) = \frac{1}{18N_z} \text{Tr} [\rho_\pm(k_y, E)], \quad (7)$$

$$\rho_{\pm,s}(k_y, E) = \frac{1}{18N_z} \text{Tr} [s_z \rho_\pm(k_y, E)], \quad (8)$$

where the normalization factor of $1/18$ is multiplied since each mirror sector has 18 bands. The spin and mirror resolved edge density of states (DOS) $\rho_{\pm,s}$ is given by

$$\rho_{\pm,\uparrow}(E) = \int \frac{dk_y}{2\pi} \frac{\rho_c(k_y, E) + \rho_s(k_y, E)}{2}, \quad (9)$$

$$\rho_{\pm,\downarrow}(E) = \int \frac{dk_y}{2\pi} \frac{\rho_c(k_y, E) - \rho_s(k_y, E)}{2}. \quad (10)$$

The calculated results for the mirror-even sector are shown in Fig. 8. The thickness is set to $N_z = 7$, where

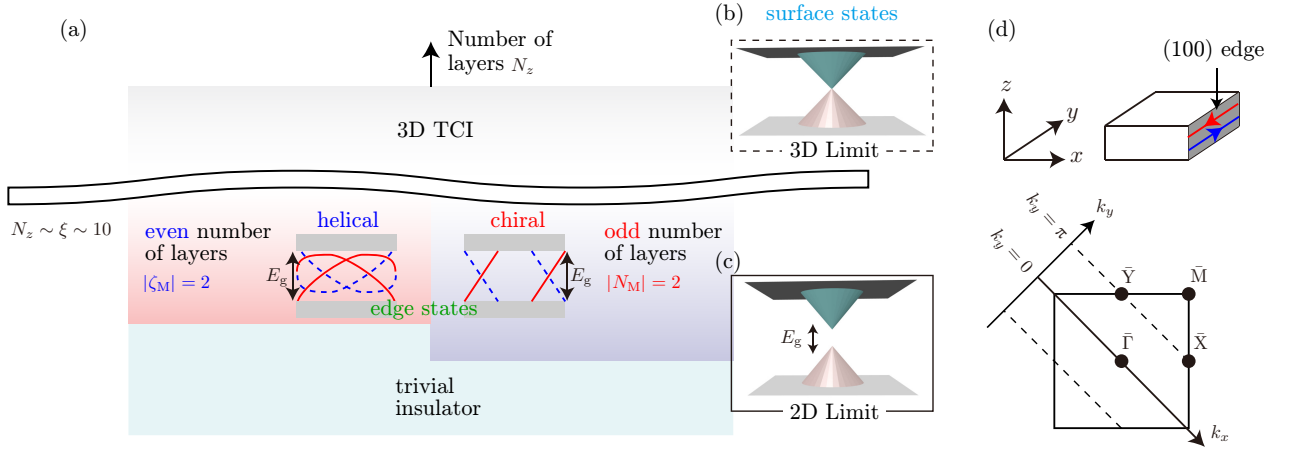


FIG. 6. Dimensional crossover (a) from three-dimensional (3D) to two-dimensional (2D) insulators in a $\text{Pb}_x\text{Sn}_{1-x}\text{Te}$ film. The two-dimensional gapless surface states (b) has a large gap in thin film of $N_z < \xi \sim 10$ (c). The mirror-Chern phase $|N_M| = 2$ supporting the mirror-chiral gapless edge states and the $|\zeta_M| = 2$ phase, which is defined by Eq. (11), supporting the mirror-helical gapless/gapful edge states, are realized for the odd and even numbers of layers, respectively. Energy dispersions of the edge states are schematically shown. The (red) solid and (blue) dashed line denote those of edge states in the mirror-even and mirror-odd sectors. In the thin limit, the system falls into a trivial insulator. The two dimensional and the projected one-dimensional BZs are illustrated in (d).

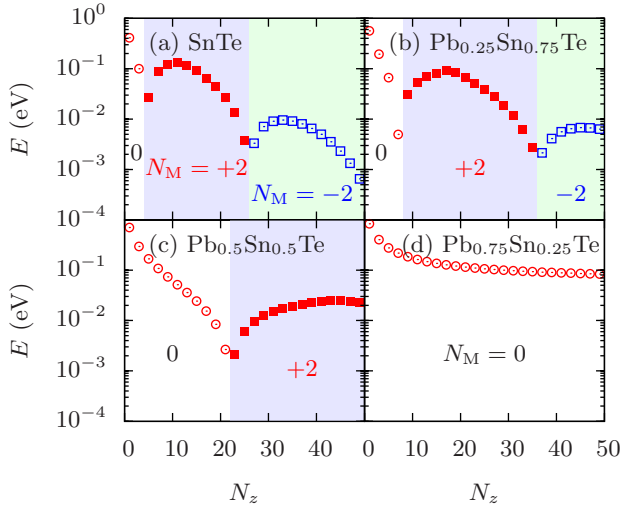


FIG. 7. Topological phase diagram in odd numbers of layers of $\text{Pb}_x\text{Sn}_{1-x}\text{Te}$. TCI with $|N_M| = 2$ is realized in the shaded regions. Energy gap is denoted by the open circles, closed squares, and open squares for non-topological insulator $N_M = 0$, TCI with $N_M = 2$, and TCI with $N_M = -2$, respectively.

the mirror Chern number is obtained to be $N_M = 2$. The charge spectral function [Fig. 8(a)] clearly show two branches of gapless mirror-chiral edge states, which are protected by the mirror Chern number $N_M = 2$. As the edge states have been expected to be spin-filtered,⁵³ we evaluate the spin spectral function [Fig. 8(b)]. This indicates that the gapless edge states in the left and right branches are composed of spin up and down, respectively. Both edge states with spin up and down can go to the same direction, i.e., the spin of edge states is not com-

pletely but partially filtered. In the edge DOS, spin polarization is estimated to be $(\rho_{+, \uparrow} - \rho_{+, \downarrow})/(\rho_{+, \uparrow} + \rho_{+, \downarrow}) \sim 0.1$ within the bulk gap as shown in Fig. 8(c).

In the present system, the (001)-reflection operator \mathcal{M} is given by $\mathcal{M}c_n\mathcal{M}^\dagger = \eta M c_{N_z+1-n}$ and $M = -iP_z s_z$ [see Eq. (1)], which depends not only on spin but also on orbitals and layer: spins of p_x - and p_y -orbitals are canceled with that of p_z -orbital in the (001)-reflection, and the reflection is nonlocal with respect to degrees of freedom of layer n . As a consequence, the (001)-reflection operator is no longer regarded as the well-defined spin. But the partially polarized z -component of spin [Fig. 8(c)] may give rise to spin transport phenomena such as spin Hall conductance. For realization of a spintronics device with TCI films, more extensive studies on the edge states is needed.

The second minima in the energy gap appear at $N_z = 25$ for SnTe [Fig. 7(a)] and at $N_z = 35$ for $\text{Pb}_{0.25}\text{Sn}_{0.75}\text{Te}$ [Fig. 7(b)]. This stems from the sign-change of the mirror Chern number at these minima, where the band gap closes simultaneously at two momenta away from the \bar{X} point. Note that there is an ambiguity on the sign of the mirror Chern number since the phase factor of the reflection operator \mathcal{M} is arbitrary. The phase is fixed to η in Eq. (1). Validity of this choice is proven by confirming the detail structure of energy dispersion for the edge states shown in Fig. 9. The finite-size-effect induced gap is located at $k_y \sim 0.91\pi$, and there exists gapless edge states within the gap. In the $N_M = 2$ phase, the group velocity of the edge state in the $M = +i$ sector is negative [Fig. 9(a) and 9(b)] near $k_y \sim 0.91\pi$. The bulk gap shows a minimum at $25 < N_z < 27$ then the group velocity becomes positive in the $N_M = -2$ phase [Fig. 9(c) and 9(d)]. The sign change of the mirror Chern

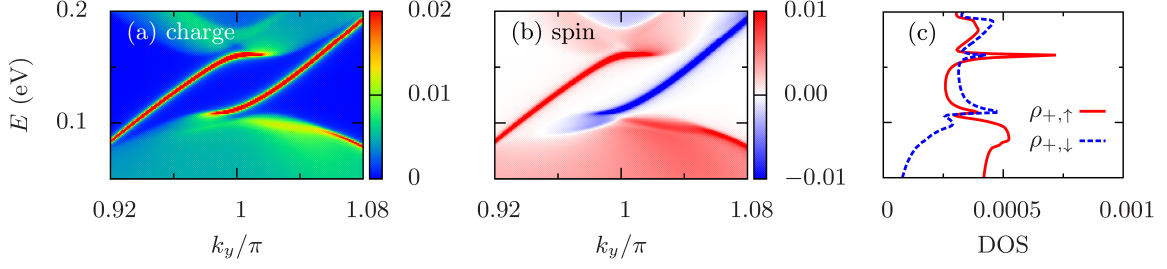


FIG. 8. The edge charge $\rho_{+,c}(k_y, E)$ (a) and spin $\rho_{+,s}(k_y, E)$ (b) spectral functions and the spin-resolved edge DOS $\rho_{+, \uparrow}(E)$ and $\rho_{+, \downarrow}(E)$ (c) for the mirror-even sector. The thickness is set to $N_z = 7$. All the vertical axes denote energy E (eV) in the same scale.

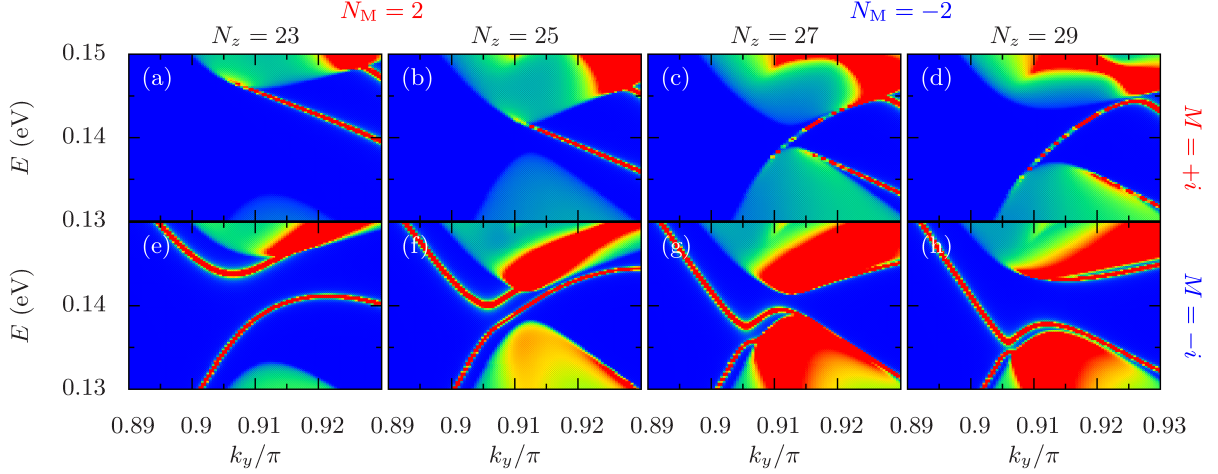


FIG. 9. Edge spectral function $\rho_{\pm,c}(k_y, E)$ for $N_z = 23$ [(a) and (e)], 25 [(b) and (f)], 27 [(c) and (g)], and 29 [(d) and (h)]. The mirror eigenvalue is given by $M = +i$ for (a)–(d) and $M = -i$ for (e)–(h). The mirror Chern number is obtained to be $N_M = 2$ for $N_z \leq 25$ and $N_M = -2$ for $N_z \geq 27$.

number captures change of the local structure of energy dispersions for the edge states, i.e., the sign of the mirror Chern number corresponds to that of the edge state in the vicinity of the bulk band gap. And also, the similar situation occurs in the $M = -i$ sector [Fig. 9(e)–9(h)]. The above discussion justifies the definition Eq. (1) and the choice of the phase factor η .

B. Even numbers of layers

1. Phase diagram

The mirror Chern number N_M vanishes in the even numbers of layers since time-reversal symmetry [see Eq. (B14)] is preserved. In stead of the mirror Chern number, a winding number ζ_M becomes nontrivial. ζ_M is defined by $\zeta_M = (\zeta_+ - \zeta_-)/2$ with

$$\zeta_{\pm} = \int_0^{2\pi} \frac{dk_y}{2\pi} \frac{\partial \theta_{\pm}(k_y)}{\partial k_y} - \frac{\theta_{\pm}(2\pi) - \theta_{\pm}(0)}{2\pi}, \quad (11)$$

and

$$\theta_{\pm}(k_y) = \text{Im} \ln \det \left\{ P \exp \left[i \int_{-\pi}^{\pi} dk_x A_{\pm}(k_x, k_y) \right] \times B_{\pm}(k_y) \right\}, \quad (12)$$

where P stands for the path-ordering. The non-Abelian Berry connection A_{\pm} is defined by^{62,63}

$$[A_{\pm}(k_x, k_y)]_{mn} = \langle k_x, k_y, \pm, m | \frac{\partial}{\partial k_x} | k_x, k_y, \pm, n \rangle, \quad (13)$$

where $|k_x, k_y, \pm, m\rangle$ is an eigenvector of the Hamiltonian $H_{\pm}(k_x, k_y)$, and m, n are the occupied band indices. Matrix $B(k_y)$, which is defined by

$$[B_{\pm}(k_y)]_{mn} = \langle \pi, k_y, \pm, m | -\pi, k_y, \pm, n \rangle, \quad (14)$$

is attached in Eq. (11) so that ζ_M is invariant for gauge transformation and symmetry operations of the system. ζ_M introduced above is a \mathbb{Z} topological invariant in two spatial dimension. This invariant is protected by translation, reflection, and time-reversal symmetries, which is

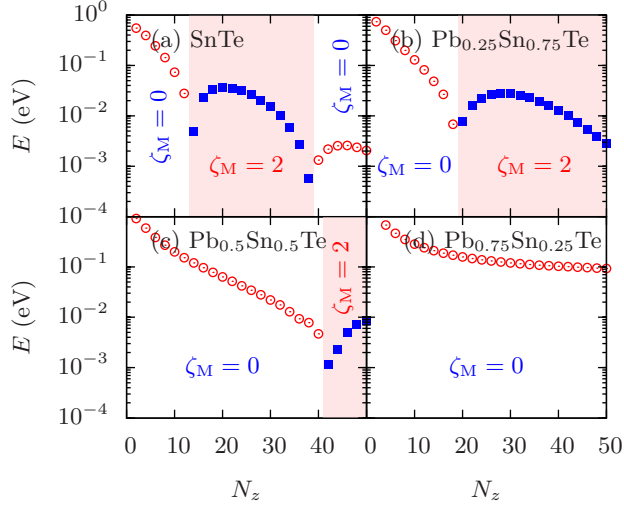


FIG. 10. Topological phase diagram in even numbers of layers of $\text{Pb}_x\text{Sn}_{1-x}\text{Te}$. Energy gap and topological invariant ζ_M are shown. $|\zeta_M| = 2$ is denoted by the closed square in the shaded region.

explained in Appendix C. A numerical recipe for ζ_M is given also in Appendix C.

The calculated topological invariant are shown in Fig. 10 with the energy gap. In the thin limit, the topological number is obtained to be $\zeta_M = 0$. As the thickness increases, the energy gap takes a minimal value at $12 < N_z < 14$ for SnTe, at $18 < N_z < 20$ for $\text{Pb}_{0.25}\text{Sn}_{0.75}$, and at $40 < N_z < 42$ for $\text{Pb}_{0.5}\text{Sn}_{0.5}\text{Te}$, when the topological number changes from $\zeta_M = 0$ to $|\zeta_M| = 2$. The change of topological invariant must be associated by bulk gap closing. This is why the energy gap exhibits minima as the thickness increases in the even numbers of layers.

2. Edge state

Here we discuss gapless one-dimensional edge states on the (100) edge [see Fig. 6(d)] in the case of $|\zeta_M| = 2$. Figure 11 shows the edge charge spectral function $\rho_{+,c}(k_y, E)$ for the mirror-even sector in the even numbers of layers of SnTe film. There are gapless mirror-helical edge states at $k_y \sim \pi$ for $|\zeta_M| = 2$. One can see degeneracy of the edge states at the zone boundary $k_y = \pi$ in Fig. 11(a), which is protected by the time-reversal symmetry defined in Appendix B3. Figure 11(b) shows the total edge-charge-spectral function $\rho_{+,c}(k_y, E) + \rho_{-,c}(k_y, E)$. Degeneracies of the edge states at $k_y \neq \pi$ are protected by the (001)-reflection symmetry. Both time-reversal and (001)-reflection symmetries are necessary for gapless edge states in the case of even numbers of layers.

The gapless edge states is, however, not robust: it is removed without bulk gap closing. As illustrated in Fig. 12, two branches can be merged and become gapped con-

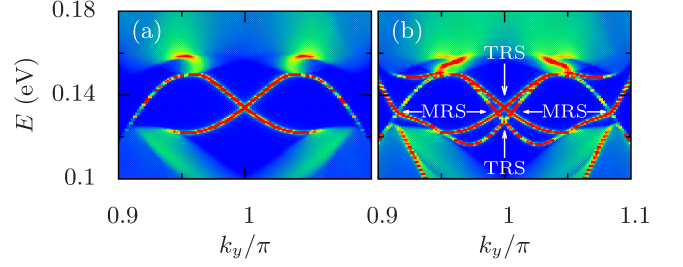


FIG. 11. One-dimensional gapless edge states along the (100) edge in SnTe film with $N_z = 20$ for (a) the mirror-even and (b) both sectors. The degeneracies denoted by the arrows are protected by mirror-reflection (MRS) and time-reversal (TRS) symmetries, respectively.

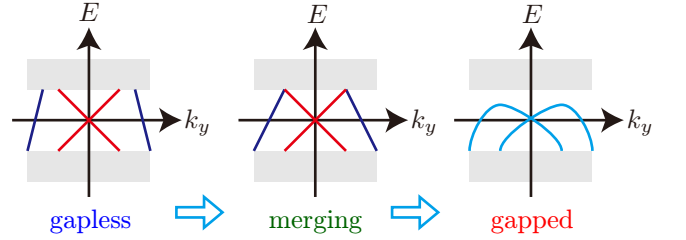


FIG. 12. Evolution from gapless to gapped edge states induced by perturbation. The energy dispersions correspond to that in Fig. 11(a).

tinuously without any gap closing. Although the system has the nontrivial topological invariant ζ_M , it has no bulk-edge correspondence. Equation (11) is a topological number protected by a complex symmetry involving spatial inversion symmetry (see Appendix C2), which is preserved in the bulk but not in the edge. Namely, a nontrivial value of ζ_M does not lead to the existence of robust gapless edge states.

The second minima of energy gap at $N_z = 40$ for the SnTe film [Fig. 7(a)] originates from the change of the topological number from $|\zeta_M| = 2$ to $\zeta_M = 0$. It follows that the local structure of energy dispersion for the edge states changes near the band gap, via bulk gap closing as explained below. Figures 13 and 14 show the edge charge spectral function for $N_z = 38$ and $N_z = 40$, in the vicinity of which the topological number changes from $|\zeta_M| = 2$ to $\zeta_M = 0$ and the band gap closes. The whole structures of energy dispersion for $N_z = 38$ [Figs. 13(a) and 13(c)] and $N_z = 40$ [Figs. 13(b) and 13(d)] are nearly the same. Near the band gap ($k_y \sim 0.912\pi$), on the other hand, gapless edge states for $N_z = 38$ [Figs. 14(a) and 14(c)] become gapped for $N_z = 40$ [Figs. 14(b) and 14(d)], accompanying the change of topological number ζ_M . The change of ζ_M can describe bulk gap closing and generation of gapless edge states, although the bulk-edge correspondence does not exactly hold.

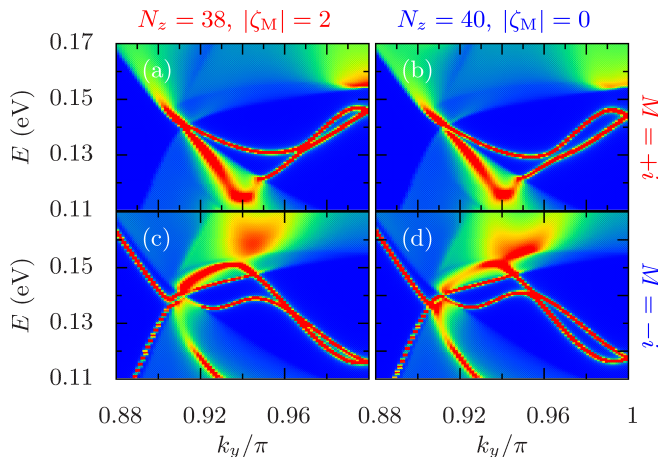


FIG. 13. Edge spectral function for $N_z = 38$ [(a) and (c)] and $N_z = 40$ [(b) and (d)]. The mirror eigenvalue is given by $M = +i$ for (a) and (b) and $M = -i$ for (c) and (d).

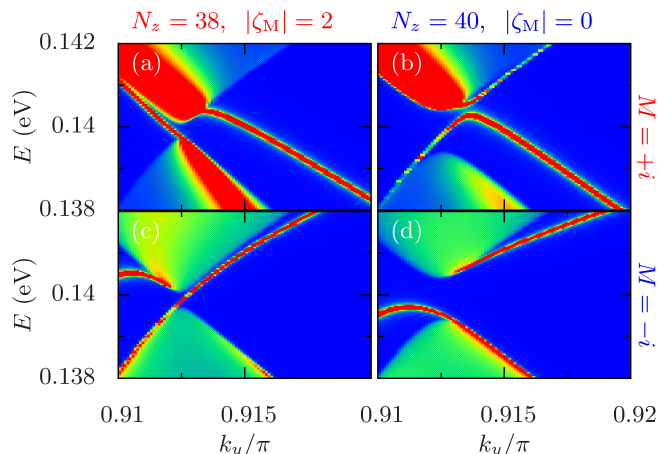


FIG. 14. Edge spectral function in the vicinity of the band gap. (a)–(d) correspond to those in Fig. 13, respectively.

C. Discussion

In the thin film, the mirror Chern insulator of $|N_M| = 2$ with robust gapless mirror-chiral edge states and $|\zeta_M| = 2$ insulator with gapless/gapful mirror-helical edge states are realized for the odd and even numbers of layers, respectively. Experimental evidence of these edge states is quantization of two-terminal charge conductance G_{xx} of the order of $G_{xx} \sim e^2/h$, e.g., $G_{xx} = 4e^2/h$ for $N_z = 7$ [Fig. 8(a)] and $G_{xx} = 8e^2/h$ for $N_z = 20$ (Fig. 11) in the ballistic limit.

What is a quantity directly related to N_M or ζ_M ? One of the candidates is mirror Hall conductance, which is defined by $G_{M,xy} = G_{+,xy} - G_{-,xy}$, where $G_{\pm,xy}$ denotes charge Hall conductance in each mirror sector. In the odd numbers of layers, the gapless mirror-chiral edge states result in the quantized mirror Hall conductance $G_{M,xy} = 2N_M e^2/h$. On the contrary, the mirror

Chern number, i.e., the mirror Hall conductance vanishes ($N_M = 0$) in the even numbers of layers since the system has time-reversal symmetry in each mirror sector and the corresponding edge states are mirror-helical. If one measure the mirror Hall conductance, the $|N_M| = 2$ and $|\zeta_M| = 2$ insulators can be distinguished from each other.

Note that it is difficult to detect the *mirror* Hall conductance experimentally since *mirror* is not observable. In single band systems, the (001)-reflection operator M can be identified to spin as $M = -is_z$, i.e., mirror Hall conductance is equivalent to spin Hall conductance. In multi-orbital systems, on the other hand, the (001)-reflection operator depends on orbitals. Spins of each orbital can be partially canceled in each mirror sector. In fact, we found that the gapless edge states in each mirror sector for the $|N_M| = 2$ phase has partial (about 10%) spin polarization. This leads to a (not quantized) finite value of z -component spin Hall conductance, which is an evidence of the $|N_M| = 2$ phase. Besides, to find phenomena directly related to the mirror Chern number is an important remaining issue.

It is also a challenging study to characterize $|\zeta_M| \neq 0$ insulators by physical quantities since it has no robust gapless edge state. The relevant system is inversion symmetric insulator in odd spatial dimensions, in which the topological number does not guarantee the existence of gapless edge states but mid-gap entanglement modes^{64,65} and the magneto-electric crossed response.⁶⁵ In this case, the topological number is equivalent to the magneto-electric polarizability.⁶⁶ Unfortunately, such a nontrivial response has not been found in even spatial dimensions. To make matters more challenging, the topological number ζ_M is protected by a combination of mirror-reflection, time-reversal, translation in the reciprocal space, and inversion symmetries. Such a crystalline topological number in even spatial dimensions also should be made a correlation to physical phenomena.

All calculations in the paper have been based on a tight-binding model which does not include the surface and edge potential effects in a self-consistent manner. In particular, surface reconstruction could be important for tiny energy gaps and small energy ranges over which the edge states exist. On the other hand, edge reconstruction is not so much important as surface reconstruction for qualitative study since the existence of edge state is guaranteed by the topological invariant in the two-dimensional bulk system. For quantitative study in the small energy scales, surface- and edge-reconstruction effects should be evaluated.

For transport measurement and device application, it is necessary to study effects of surface roughness of the film. We have shown the non-monotonically thickness-dependent energy gap and two-dimensional topological number. The even numbers of layers has the topological number different from that of the odd numbers of layers. These suggest that surface roughness can crucially affect the topological phase and resulting transport phenom-

ena. This issue should be discussed elsewhere.

Furthermore, recently, nanowires of SnTe have been synthesized.^{67,68} Finite-size effect of one-dimensional SnTe wires, which is natural extension of the present work, will be discussed in future work.

IV. SUMMARY

In summary, we have elucidated electronic states and topological invariants in a TCI $\text{Pb}_x\text{Sn}_{1-x}\text{Te}$ film. Energy gap of the film shows damped oscillation as a function of the thickness. We have also clarified that the oscillation of energy gap originates from the change of topological number from trivial to \mathbb{Z} invariants. This structure is richer than that of \mathbb{Z}_2 TIs such as Bi_2Se_3 , in which only \mathbb{Z}_2 phase can be realized in the film. In contrast, the topological numbers of the TCI film can be tuned to the (signed) mirror Chern number $N_M = \pm 2$, and also to $|\zeta_M| = 2$, by tuning the number of layers of film. The obtained data may provide essential support for understanding electronic states and transport properties of the film, which depend non-monotonically on the number of layers.

ACKNOWLEDGMENTS

The authors are grateful to Y. Ando, S. Onari, T. Hashimoto, K. Yada, M. Ezawa, and S. Kashiwaya for fruitful discussions. This work is supported by the “Topological Quantum Phenomena” (no. 22103005) Grant-in Aid for Scientific Research on Innovative Areas from the Ministry of Education, Culture, Sports, Science and Technology (MEXT) of Japan. M.S. is supported by Grant-in-Aid for Scientific Research B (no. 25287085) from Japan Society for the Promotion of Science (JSPS).

Appendix A: Model

1. (001)-film based on the 36×36 model

Based on the 36×36 model,⁵⁹ we construct a model for (001)-film of IV-VI semiconductors as

$$H = \sum_{n_z=1}^{N_z} \mathbf{c}_{n_z}^\dagger \epsilon \mathbf{c}_{n_z} + \sum_{n_z=1}^{N_z-1} (\mathbf{c}_{n_z}^\dagger t_z \mathbf{c}_{n_z+1} + \text{H.c.}). \quad (\text{A1})$$

36×36 matrices ϵ and t_z are obtained from the bulk Hamiltonian with the substitutions of $2 \cos k_z/2 \rightarrow \mathbf{c}_n^\dagger \mathbf{c}_{n+1} + \mathbf{c}_{n+1}^\dagger \mathbf{c}_n$ and $2i \sin k_z/2 \rightarrow \mathbf{c}_n^\dagger \mathbf{c}_{n+1} - \mathbf{c}_{n+1}^\dagger \mathbf{c}_n$.

The explicit forms of ϵ and t_z are given by

$$\epsilon = \begin{pmatrix} \epsilon_{ss} & \epsilon_{pcs}^\dagger & \epsilon_{pas}^\dagger & 0 & 0 \\ \epsilon_{pcs} & \epsilon_{pcpc} & \epsilon_{papc}^\dagger & 0 & \epsilon_{dapc}^\dagger \\ \epsilon_{pas} & \epsilon_{papc} & \epsilon_{papa} & \epsilon_{dcpc}^\dagger & 0 \\ 0 & 0 & \epsilon_{dcpc} & \epsilon_{dcdc} & \epsilon_{dadc}^\dagger \\ 0 & \epsilon_{dapc} & 0 & \epsilon_{dadc} & \epsilon_{dada} \end{pmatrix}, \quad (\text{A2})$$

$$t_z = \begin{pmatrix} t_{ss} & -t_{pcs}^T & -t_{pas}^T & 0 & 0 \\ t_{pcs} & 0 & t_{papc} & 0 & -t_{dapc}^T \\ t_{pas} & t_{papc} & 0 & -t_{dcpc}^T & 0 \\ 0 & 0 & t_{dcpc} & 0 & t_{dadc} \\ 0 & t_{dapc} & 0 & t_{dadc} & 0 \end{pmatrix}, \quad (\text{A3})$$

with

$$\epsilon_{ss} = \begin{pmatrix} E_{sc} & 0 & c_0 V_{ss} & 0 \\ 0 & E_{sc} & 0 & c_0 V_{ss} \\ c_0 V_{ss} & 0 & E_{sa} & 0 \\ 0 & c_0 V_{ss} & 0 & E_{sa} \end{pmatrix}, \quad (\text{A4})$$

$$\epsilon_{pcs} = \begin{pmatrix} 0 & 0 & -2s_x V_{ps} & 0 \\ 0 & 0 & -2s_y V_{ps} & 0 \\ 0 & 0 & 0 & 0 \\ 0 & 0 & 0 & -2s_x V_{ps} \\ 0 & 0 & 0 & -2s_y V_{ps} \\ 0 & 0 & 0 & 0 \end{pmatrix}, \quad (\text{A5})$$

$$\epsilon_{pas} = \begin{pmatrix} -2s_x V_{sp} & 0 & 0 & 0 \\ -2s_y V_{sp} & 0 & 0 & 0 \\ 0 & 0 & 0 & 0 \\ 0 & -2s_x V_{sp} & 0 & 0 \\ 0 & -2s_y V_{sp} & 0 & 0 \\ 0 & 0 & 0 & 0 \end{pmatrix}, \quad (\text{A6})$$

$$\epsilon_{pcpc} = \begin{pmatrix} E_{pc} & -i\frac{\lambda_c}{2} & 0 & 0 & 0 & \frac{\lambda_c}{2} \\ i\frac{\lambda_c}{2} & E_{pc} & 0 & 0 & 0 & -i\frac{\lambda_c}{2} \\ 0 & 0 & E_{pc} & -\frac{\lambda_c}{2} & i\frac{\lambda_c}{2} & 0 \\ 0 & 0 & -\frac{\lambda_c}{2} & E_{pc} & i\frac{\lambda_c}{2} & 0 \\ 0 & 0 & -i\frac{\lambda_c}{2} & -i\frac{\lambda_c}{2} & E_{pc} & 0 \\ \frac{\lambda_c}{2} & i\frac{\lambda_c}{2} & 0 & 0 & 0 & E_{pc} \end{pmatrix}, \quad (\text{A7})$$

$$\epsilon_{papa} = \epsilon_{pcpc}|_{E_{pc} \rightarrow E_{pa}, \lambda_c \rightarrow \lambda_a}, \quad (\text{A8})$$

$$\epsilon_{papc} = \text{diag}(W_x, W_y, c_0 V_{pp\pi}, W_x, W_y, c_0 V_{pp\pi}), \quad (\text{A9})$$

$$\epsilon_{dapc} = \text{diag}(\epsilon_5, \epsilon_5), \quad (\text{A10})$$

$$\epsilon_5 = \begin{pmatrix} -\sqrt{3}s_x V_{pd} & \sqrt{3}s_y V_{pd} & 0 \\ s_x V_{pd} & s_y V_{pd} & 0 \\ -2s_y V_{pd\pi} & -2s_x V_{pd\pi} & 0 \\ 0 & 0 & -2s_y V_{pd\pi} \\ 0 & 0 & -2s_x V_{pd\pi} \end{pmatrix}, \quad (\text{A11})$$

$$\epsilon_{\text{dcpa}} = \epsilon_{\text{dapc}}|_{V_{\text{pd}} \rightarrow V_{\text{dp}}, V_{\text{pd}\pi} \rightarrow V_{\text{dp}\pi}}. \quad (\text{A12})$$

10×10 matrix ϵ_{dadc} has ten nonzero diagonal and four nonzero off-diagonal elements given by

$$(\epsilon_{\text{dadc}})_{1,1} = (\epsilon_{\text{dadc}})_{6,6} = (c_x + c_y) \frac{3V_{\text{dd}} + V_{\text{dd}\delta}}{2}, \quad (\text{A13})$$

$$(\epsilon_{\text{dadc}})_{2,2} = (\epsilon_{\text{dadc}})_{7,7} = (c_x + c_y) \frac{3V_{\text{dd}\delta} + V_{\text{dd}}}{2}, \quad (\text{A14})$$

$$(\epsilon_{\text{dadc}})_{3,3} = (\epsilon_{\text{dadc}})_{8,8} = c_0 V_{\text{dd}\pi}, \quad (\text{A15})$$

$$(\epsilon_{\text{dadc}})_{4,4} = (\epsilon_{\text{dadc}})_{9,9} = 2c_y V_{\text{dd}\pi} + 2c_x V_{\text{dd}\delta}, \quad (\text{A16})$$

$$(\epsilon_{\text{dadc}})_{5,5} = (\epsilon_{\text{dadc}})_{10,10} = 2c_x V_{\text{dd}\pi} + 2c_y V_{\text{dd}\delta}, \quad (\text{A17})$$

$$\begin{aligned} (\epsilon_{\text{dadc}})_{1,2} &= (\epsilon_{\text{dadc}})_{2,1} = (\epsilon_{\text{dadc}})_{6,7} = (\epsilon_{\text{dadc}})_{7,6} \\ &= \frac{\sqrt{3}}{2} (c_y - c_x) (V_{\text{dd}} - V_{\text{dd}\delta}), \end{aligned} \quad (\text{A18})$$

and

$$c_0 = 2 \cos \frac{k_x}{2} + 2 \cos \frac{k_y}{2}, \quad (\text{A19})$$

$$c_i = \cos \frac{k_i}{2}, \quad s_i = i \sin \frac{k_i}{2}, \quad (\text{A20})$$

$$W_i = 2 \cos \frac{k_i}{2} V_{\text{pp}} + 2 \cos \frac{k_j}{2} V_{\text{pp}\pi}, \quad (\text{A21})$$

where $i, j = x, y$ and $i \neq j$. ϵ_{dcdc} and ϵ_{dada} are 10×10 diagonal matrices whose elements are given by E_{dc} and E_{da} , respectively. Matrix t_z is given by

$$t_{\text{ss}} = \begin{pmatrix} 0 & 0 & V_{\text{ss}} & 0 \\ 0 & 0 & 0 & V_{\text{ss}} \\ V_{\text{ss}} & 0 & 0 & 0 \\ 0 & V_{\text{ss}} & 0 & 0 \end{pmatrix}, \quad (\text{A22})$$

$$t_{\text{pcs}} = \begin{pmatrix} 0 & 0 & 0 & 0 \\ 0 & 0 & 0 & 0 \\ 0 & 0 & -V_{\text{ps}} & 0 \\ 0 & 0 & 0 & 0 \\ 0 & 0 & 0 & 0 \\ 0 & 0 & 0 & -V_{\text{ps}} \end{pmatrix}, \quad (\text{A23})$$

$$t_{\text{pas}} = \begin{pmatrix} 0 & 0 & 0 & 0 \\ 0 & 0 & 0 & 0 \\ -V_{\text{sp}} & 0 & 0 & 0 \\ 0 & 0 & 0 & 0 \\ 0 & 0 & 0 & 0 \\ 0 & -V_{\text{sp}} & 0 & 0 \end{pmatrix}, \quad (\text{A24})$$

$$t_{\text{papc}} = \text{diag}(V_{\text{pp}\pi}, V_{\text{pp}\pi}, V_{\text{pp}}, V_{\text{pp}\pi}, V_{\text{pp}\pi}, V_{\text{pp}}), \quad (\text{A25})$$

$$t_{\text{dapc}} = \text{diag}(t_5, t_5), \quad (\text{A26})$$

$$t_5 = \begin{pmatrix} 0 & 0 & 0 \\ 0 & 0 & -V_{\text{pd}} \\ 0 & 0 & 0 \\ 0 & -V_{\text{pd}\pi} & 0 \\ -V_{\text{pd}\pi} & 0 & 0 \end{pmatrix}, \quad (\text{A27})$$

$$t_{\text{dcpa}} = t_{\text{dapc}}|_{V_{\text{pd}} \rightarrow V_{\text{dp}}, V_{\text{pd}\pi} \rightarrow V_{\text{dp}\pi}}, \quad (\text{A28})$$

$$t_{\text{dadc}} = \text{diag}(V_{\text{dd}\delta}, V_{\text{dd}}, V_{\text{dd}\delta}, V_{\text{dd}\pi}, V_{\text{dd}\pi}, V_{\text{dd}\delta}, V_{\text{dd}}, V_{\text{dd}\delta}, V_{\text{dd}\pi}, V_{\text{dd}\pi}). \quad (\text{A29})$$

Here, the basis is taken to be $(|s, c, \uparrow\rangle, |s, c, \downarrow\rangle, |s, a, \uparrow\rangle, |s, a, \downarrow\rangle, |p_x, c, \uparrow\rangle, |p_y, c, \uparrow\rangle, |p_z, c, \uparrow\rangle, |p_x, c, \downarrow\rangle, |p_y, c, \downarrow\rangle, |p_z, c, \downarrow\rangle, |p_x, a, \uparrow\rangle, |p_y, a, \uparrow\rangle, |p_z, a, \uparrow\rangle, |p_x, a, \downarrow\rangle, |p_y, a, \downarrow\rangle, |p_z, a, \downarrow\rangle, |d_{x^2-y^2}, c, \uparrow\rangle, |d_{3z^2-r^2}, c, \uparrow\rangle, |d_{xy}, c, \uparrow\rangle, |d_{yz}, c, \uparrow\rangle, |d_{zx}, c, \uparrow\rangle, |d_{x^2-y^2}, c, \downarrow\rangle, |d_{3z^2-r^2}, c, \downarrow\rangle, |d_{xy}, c, \downarrow\rangle, |d_{yz}, c, \downarrow\rangle, |d_{zx}, c, \downarrow\rangle, |d_{x^2-y^2}, a, \uparrow\rangle, |d_{3z^2-r^2}, a, \uparrow\rangle, |d_{xy}, a, \uparrow\rangle, |d_{yz}, a, \uparrow\rangle, |d_{zx}, a, \uparrow\rangle, |d_{x^2-y^2}, a, \downarrow\rangle, |d_{3z^2-r^2}, a, \downarrow\rangle, |d_{xy}, a, \downarrow\rangle, |d_{yz}, a, \downarrow\rangle, |d_{zx}, a, \downarrow\rangle)$. In the actual calculations, the parameters are taken from Ref. 59.

2. Model for (001)-film with (100)-edge

A model Hamiltonian for the film with (100)-edge can be obtained in a similar manner to the previous case: substitution of $2 \cos k_x/2 \rightarrow c_{n_x, n_z}^\dagger(k_y) c_{n_x+1, n_z}(k_y) + c_{n_x+1, n_z}^\dagger(k_y) c_{n_x, n_z}(k_y)$ and $2i \sin k_x/2 \rightarrow c_{n_x, n_z}^\dagger(k_y) c_{n_x+1, n_z}(k_y) - c_{n_x+1, n_z}^\dagger(k_y) c_{n_x, n_z}(k_y)$. The resulting Hamiltonian has the form as

$$\begin{aligned} \tilde{H} &= \sum_{n_z=1}^{N_z} \sum_{n_x=1}^{N_x} c_{n_z, n_x}^\dagger \tilde{\epsilon} c_{n_z, n_x} \\ &+ \sum_{n_z=1}^{N_z-1} \sum_{n_x=1}^{N_x} c_{n_z, n_x}^\dagger t_z c_{n_z+1, n_x} + \text{H.c.} \\ &+ \sum_{n_z=1}^{N_z} \sum_{n_x=1}^{N_x-1} c_{n_z, n_x}^\dagger \tilde{t}_x c_{n_z, n_x+1} + \text{H.c.} \end{aligned} \quad (\text{A30})$$

The on-site energy $\tilde{\epsilon}$ is given by

$$\tilde{\epsilon} = \begin{pmatrix} \tilde{\epsilon}_{\text{ss}} & \tilde{\epsilon}_{\text{pcs}}^\dagger & \tilde{\epsilon}_{\text{pas}}^\dagger & 0 & 0 \\ \tilde{\epsilon}_{\text{pcs}} & \epsilon_{\text{pcpc}} & \tilde{\epsilon}_{\text{papc}}^\dagger & 0 & \tilde{\epsilon}_{\text{dapc}}^\dagger \\ \tilde{\epsilon}_{\text{pas}} & \tilde{\epsilon}_{\text{papc}} & \epsilon_{\text{papa}} & \tilde{\epsilon}_{\text{dcpa}}^\dagger & 0 \\ 0 & 0 & \tilde{\epsilon}_{\text{dcpa}} & \tilde{\epsilon}_{\text{dcdc}} & \tilde{\epsilon}_{\text{dadc}}^\dagger \\ 0 & \tilde{\epsilon}_{\text{dapc}} & 0 & \tilde{\epsilon}_{\text{dadc}} & \tilde{\epsilon}_{\text{dada}} \end{pmatrix}, \quad (\text{A31})$$

with

$$\tilde{\epsilon}_{ss} = \begin{pmatrix} E_{sc} & 0 & 2c_y V_{ss} & 0 \\ 0 & E_{sc} & 0 & 2c_y V_{ss} \\ 2c_y V_{ss} & 0 & E_{sa} & 0 \\ 0 & 2c_y V_{ss} & 0 & E_{sa} \end{pmatrix}, \quad (\text{A32})$$

$$\tilde{\epsilon}_{pcs} = \begin{pmatrix} 0 & 0 & 0 & 0 \\ 0 & 0 & -2s_y V_{ps} & 0 \\ 0 & 0 & 0 & 0 \\ 0 & 0 & 0 & 0 \\ 0 & 0 & 0 & -2s_y V_{ps} \\ 0 & 0 & 0 & 0 \end{pmatrix}, \quad (\text{A33})$$

$$\tilde{\epsilon}_{pas} = \begin{pmatrix} 0 & 0 & 0 & 0 \\ -2s_y V_{sp} & 0 & 0 & 0 \\ 0 & 0 & 0 & 0 \\ 0 & 0 & 0 & 0 \\ 0 & -2s_y V_{sp} & 0 & 0 \\ 0 & 0 & 0 & 0 \end{pmatrix}, \quad (\text{A34})$$

$$\tilde{\epsilon}_{pabc} = 2c_y \text{diag}(V_{pp\pi}, V_{pp}, V_{pp\pi}, V_{pp\pi}, V_{pp}, V_{pp\pi}), \quad (\text{A35})$$

$$\tilde{\epsilon}_{dabc} = \text{diag}(\tilde{\epsilon}_5, \tilde{\epsilon}_5), \quad (\text{A36})$$

$$\tilde{\epsilon}_5 = \begin{pmatrix} 0 & \sqrt{3}s_y V_{pd} & 0 \\ 0 & s_y V_{pd} & 0 \\ -2s_y V_{pd\pi} & 0 & 0 \\ 0 & 0 & -2s_2 V_{pd\pi} \\ 0 & 0 & 0 \end{pmatrix}, \quad (\text{A37})$$

$$\tilde{\epsilon}_{dcpa} = \tilde{\epsilon}_{dabc}|_{V_{pd} \rightarrow V_{dp}, V_{pd\pi} \rightarrow V_{dp\pi}}. \quad (\text{A38})$$

$$(\tilde{\epsilon}_{dadc})_{1,1} = (\tilde{\epsilon}_{dadc})_{6,6} = c_y \frac{3V_{dd} + V_{dd\delta}}{2}, \quad (\text{A39})$$

$$(\tilde{\epsilon}_{dadc})_{2,2} = (\tilde{\epsilon}_{dadc})_{7,7} = c_y \frac{3V_{dd\delta} + V_{dd}}{2}, \quad (\text{A40})$$

$$(\tilde{\epsilon}_{dadc})_{3,3} = (\tilde{\epsilon}_{dadc})_{8,8} = 2c_y V_{dd\pi}, \quad (\text{A41})$$

$$(\tilde{\epsilon}_{dadc})_{4,4} = (\tilde{\epsilon}_{dadc})_{9,9} = 2c_y V_{dd\pi}, \quad (\text{A42})$$

$$(\tilde{\epsilon}_{dadc})_{5,5} = (\tilde{\epsilon}_{dadc})_{10,10} = 2c_y V_{dd\delta}, \quad (\text{A43})$$

$$\begin{aligned} (\tilde{\epsilon}_{dadc})_{1,2} &= (\tilde{\epsilon}_{dadc})_{2,1} = (\tilde{\epsilon}_{dadc})_{6,7} = (\tilde{\epsilon}_{dadc})_{7,6} \\ &= \frac{\sqrt{3}}{2} c_y (V_{dd} - V_{dd\delta}). \end{aligned} \quad (\text{A44})$$

The hopping along (001)-direction t_z is the same as that defined in the previous section. The hopping along (100)-direction t_x is given by

$$t_x = \begin{pmatrix} t_{ss} & -t_{x,pcs}^T & -t_{x,pas}^T & 0 & 0 \\ t_{x,pcs} & 0 & t_{x,papc} & 0 & -t_{x,dapc}^T \\ t_{x,pas} & t_{x,papc} & 0 & -t_{x,dcpa}^T & 0 \\ 0 & 0 & t_{x,dcpa} & 0 & t_{x,dadc} \\ 0 & t_{x,dapc} & 0 & t_{x,dadc} & 0 \end{pmatrix}, \quad (\text{A45})$$

with t_{ss} defined by Eq. (A22) and

$$t_{x,pcs} = \begin{pmatrix} 0 & 0 & -V_{ps} & 0 \\ 0 & 0 & 0 & 0 \\ 0 & 0 & 0 & 0 \\ 0 & 0 & 0 & -V_{ps} \\ 0 & 0 & 0 & 0 \\ 0 & 0 & 0 & 0 \end{pmatrix}, \quad (\text{A46})$$

$$t_{x,pas} = \begin{pmatrix} -V_{sp} & 0 & 0 & 0 \\ 0 & 0 & 0 & 0 \\ 0 & 0 & 0 & 0 \\ 0 & -V_{sp} & 0 & 0 \\ 0 & 0 & 0 & 0 \\ 0 & 0 & 0 & 0 \end{pmatrix}, \quad (\text{A47})$$

$$t_{x,papc} = \text{diag}(V_{pp}, V_{pp\pi}, V_{pp\pi}, V_{pp}, V_{pp\pi}, V_{pp\pi}), \quad (\text{A48})$$

$$t_{x,dapc} = \text{diag}(t_{x,5}, t_{x,5}), \quad (\text{A49})$$

$$t_{x,5} = \begin{pmatrix} -\sqrt{3}V_{pd}/2 & 0 & 0 \\ V_{pd}/2 & 0 & 0 \\ 0 & -V_{pd\pi} & 0 \\ 0 & 0 & 0 \\ 0 & 0 & -V_{pd\pi} \end{pmatrix}, \quad (\text{A50})$$

$$t_{x,dcpa} = t_{x,dapc}|_{V_{pd} \rightarrow V_{dp}, V_{pd\pi} \rightarrow V_{dp\pi}}, \quad (\text{A51})$$

$$(t_{x,dadc})_{1,1} = (t_{x,dadc})_{6,6} = \frac{3V_{dd} + V_{dd\delta}}{4}, \quad (\text{A52})$$

$$(t_{x,dadc})_{2,2} = (t_{x,dadc})_{7,7} = \frac{3V_{dd\delta} + V_{dd}}{4}, \quad (\text{A53})$$

$$(t_{x,dadc})_{3,3} = (t_{x,dadc})_{8,8} = V_{dd\pi}, \quad (\text{A54})$$

$$(t_{x,dadc})_{4,4} = (t_{x,dadc})_{9,9} = V_{dd\delta}, \quad (\text{A55})$$

$$(t_{x,dadc})_{5,5} = (t_{x,dadc})_{10,10} = V_{dd\pi}, \quad (\text{A56})$$

$$\begin{aligned} (t_{x,dadc})_{1,2} &= (t_{x,dadc})_{2,1} = (t_{x,dadc})_{6,7} = (t_{x,dadc})_{7,6} \\ &= -\frac{\sqrt{3}}{4} (V_{dd} - V_{dd\delta}). \end{aligned} \quad (\text{A57})$$

3. (111)-film of Bi₂Se₃

Here we supply a tight-binding model of (111)-film of TI Bi₂Se₃. The Hamiltonian in low-energy region consists of two orbitals and spins as³⁸

$$H_{\text{TI}} = \sum_{n=1}^{N_z} c_n^\dagger \epsilon_{\text{TI}} c_n + \left(\sum_{n=1}^{N_z-1} c_n^\dagger t_{z,\text{TI}} c_{n+1} + \text{h.c.} \right), \quad (\text{A58})$$

with

$$\epsilon_{\text{TI}} = \begin{pmatrix} C + M & 0 & B \sin k_z c & A_- \\ 0 & C + M & A_+ & -B \sin k_z c \\ B \sin k_z c & A_- & C - M & 0 \\ A_+ & -B \sin k_z c & 0 & C - M \end{pmatrix}, \quad (\text{A59})$$

# of layer	even	odd
class	AII-R ₊	AII-R ₋
	$[\hat{\Theta}_{\bar{x}}, \sqrt{\mathcal{M}^2} \mathcal{M}] = 0$	$\{\hat{\Theta}, \sqrt{\mathcal{M}^2} \mathcal{M}\} = 0$
period	4π	2π
Kramers	\bar{X}, \bar{M}	no
inversion	yes	yes

TABLE I. Summary of symmetries of the film. Symmetry classes of the even and odd numbers of layers are AII-R₊ and AII-R₋ defined in Refs. 69 and 70, respectively. Time-reversal operators $\hat{\Theta}$ and $\hat{\Theta}_{\bar{x}}$ are defined in Appendix B 3. \mathcal{M}^2 is proportional to the identity matrix. Period in the momentum space, position of Kramers pair (time-reversal invariant momentum), are summarized for the even and odd numbers of layers in each mirror sector.

$$t_{z\text{TI}} = \begin{pmatrix} -M_1 - C_1 & 0 & iB/2 & 0 \\ 0 & -M_1 - C_1 & 0 & -iB/2 \\ iB/2 & 0 & M_1 - C_1 & 0 \\ 0 & -iB/2 & 0 & M_1 - C_1 \end{pmatrix}, \quad (\text{A60})$$

$$C = 2C_1 + C_2(2 - \cos k_x a - \cos k_y a), \quad (\text{A61})$$

$$M = M_0 + 2M_1 + M_2(2 - \cos k_x a - \cos k_y a), \quad (\text{A62})$$

$$A_{\pm} = A(\sin k_x a \pm i \sin k_y a), \quad (\text{A63})$$

where N_z is the number of the quintuple layers of film, and the basis is taken as $(|+, \uparrow\rangle, |+, \downarrow\rangle, |-, \uparrow\rangle, |-, \downarrow\rangle)$, in which \pm and \uparrow/\downarrow denote the parity eigenvalue of the orbital and spin respectively. The parameters for Bi₂Se₃ are evaluated as follows,³⁸ $M_0 = -0.28\text{eV}$, $M_1 = 0.216\text{eV}$, $M_2 = 2.60\text{eV}$, $A = 0.80\text{eV}$, $B = 0.32\text{eV}$, $C_1 = 0.024\text{eV}$, $C_2 = 1.77\text{eV}$, $a = 4.14\text{\AA}$, and $c = 9.55\text{\AA}$. In the model the crystal structure is approximated to be cubic while the actual structure is rhombohedral, since the difference does not alter the long-wavelength physics.

Appendix B: Symmetry

Symmetries of the film is different from those of the three-dimensional bulk system. Moreover, the even and odd numbers of layers have different symmetries. The result is summarized in TABLE I.

1. (001)–reflection symmetry

First, we start with (001)–reflection symmetry, which is satisfied in both the even and odd numbers of layers. The Hamiltonian has the form

$$H(\mathbf{k}) = \sum_{n=1}^{N_z} c_n^\dagger(\mathbf{k}) \epsilon(\mathbf{k}) c_n(\mathbf{k}) + \sum_{n=1}^{N_z-1} \left[c_n^\dagger(\mathbf{k}) t_z c_{n+1}(\mathbf{k}) + c_{n+1}^\dagger(\mathbf{k}) t_z^\dagger c_n(\mathbf{k}) \right], \quad (\text{B1})$$

where $\mathbf{k} = (k_x, k_y)$, matrices ϵ and t_z are defined in Appendix A 1. ϵ and t_z are transformed by (001)–reflection, as follows,

$$M\epsilon(\mathbf{k})M^\dagger = \epsilon(\mathbf{k}), \quad Mt_z M^\dagger = t_z^\dagger. \quad (\text{B2})$$

(001)–reflection operator M is given by $M = -iP_z s_z$, where P_z is the $z \rightarrow -z$ operator acting on the orbital space and s_z is the z –component of spin. From the above relations, one finds the (001)–reflection symmetry $\mathcal{M}H(\mathbf{k})\mathcal{M}^\dagger = H(\mathbf{k})$ with

$$\mathcal{M}c_n(\mathbf{k})\mathcal{M}^\dagger = \eta M c_{N_z+1-n}(\mathbf{k}), \quad (\text{B3})$$

where phase factor η is defined in Eq. (1). Note that the above discussion is applied also for the even numbers of layers, nevertheless the actual lattice with even number of layers does not have (001)–reflection symmetry. This is because the system has in-plane translational symmetry. The Hamiltonian H is expressed in the momentum (k_x, k_y) space so that the translational symmetry is implemented in H . Namely, the microscopic positions of cation and anion are no longer distinguished in $H(k_x, k_y)$. In this sense, the even number of layers has the (001)–reflection symmetry.

With the help of the (001)–reflection symmetry, Hamiltonian H can be decomposed into two mirror sectors:

$$H = H_+ \oplus H_-, \quad H_{\pm} = P_{\pm} H P_{\pm}, \quad (\text{B4})$$

with the mirror-projection operator $P_{\pm} = \sum_m |m, \pm\rangle \langle m, \pm|$, $\mathcal{M}|m, \pm\rangle = \pm|m, \pm\rangle$, and $|m, \pm\rangle$ denotes the m –th eigenvector of H_{\pm} .

2. Periodicity

The projected Brillouin zone is given by $|k_y| \leq 2\pi - |k_x|$, $k_x \in [-2\pi, 2\pi]$. The reciprocal lattice vectors are defined by $\mathbf{G}_1 = 2\pi(\mathbf{e}_x + \mathbf{e}_y)$ and $\mathbf{G}_2 = 2\pi(-\mathbf{e}_x + \mathbf{e}_y)$ with $\mathbf{e}_x = (1, 0)$ and $\mathbf{e}_y = (0, 1)$. However, the Hamiltonian does not have the trivial periodicity: $H(\mathbf{k}) \neq H(\mathbf{k} + \mathbf{G}_i)$. In order to retain the periodicity, a gauge transformation U is needed. Periodicity of ϵ and t_z gives following relations,

$$\epsilon(\mathbf{k}) = U\epsilon(\mathbf{k} + \mathbf{G}_i)U^\dagger, \quad t_z = -Ut_z U^\dagger, \quad (\text{B5})$$

where U is the operator giving a negative sign to wave functions of the anions. Consequently, periodicity of the film is satisfied as

$$H(\mathbf{k}) = \mathcal{U}H(\mathbf{k} + \mathbf{G}_i)\mathcal{U}^\dagger, \quad (\text{B6})$$

with

$$\mathcal{U}c_n(\mathbf{k})\mathcal{U}^\dagger = (-1)^n U c_n(\mathbf{k} + \mathbf{G}_i). \quad (\text{B7})$$

The negative sign factor changes the periodicity in each mirror sector: in the case of odd (even) numbers of layers, \mathcal{U} (anti)commutes with \mathcal{M} .

$$\mathcal{M}\mathcal{U} + (-1)^{N_z} \mathcal{U}\mathcal{M} = 0. \quad (\text{B8})$$

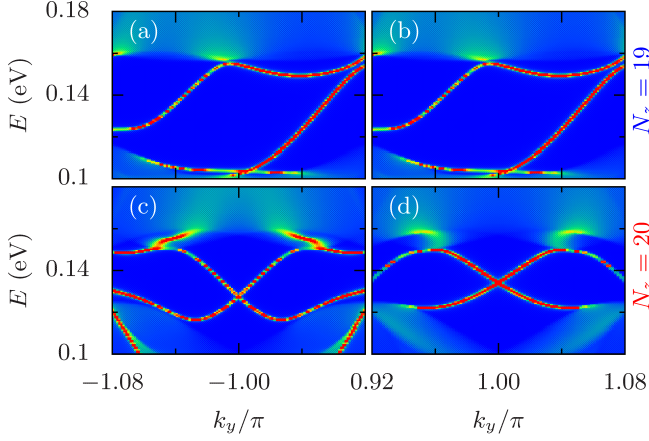


FIG. 15. 2π [(a) and (b)] and 4π [(c) and (d)] periodicities of energy dispersion in each mirror sector. Edge spectral function for $N_z = 19$ [(a) and (b)] and for $N_z = 20$ [(c) and (d)] of SnTe film. (a) and (c) [(b) and (d)] show those around $k_y = -\pi$ ($k_y = \pi$).

Thus 2π periodicity $H_{\pm}(\mathbf{k}) = \mathcal{U}H_{\pm}(\mathbf{k} + \mathbf{G}_i)\mathcal{U}^{\dagger}$ is satisfied only for the odd numbers of layers. On the other hand, for the even numbers of layers, the Hamiltonian has the doubled periodicity

$$H_{\pm}(\mathbf{k}) = \mathcal{U}H_{\mp}(\mathbf{k} + \mathbf{G}_i)\mathcal{U}^{\dagger} = H_{\pm}(\mathbf{k} + \mathbf{G}_1 + \mathbf{G}_2). \quad (\text{B9})$$

The periodicities can be directly confirmed in the (10)-edge spectral functions shown in Fig. 15. The edge spectral function for the odd numbers of layers in $-2\pi \leq k_y \leq 0$ [Fig. 15(a)] takes the same value as that in $0 \leq k_y \leq 2\pi$ [Fig. 15(b)], i.e., the period is 2π . On the other hand, for the even numbers of layers, those in $-2\pi \leq k_y \leq 0$ [Fig. 15(c)] and in $0 \leq k_y \leq 2\pi$ [Fig. 15(d)] are different, i.e., the resulting period is given by not 2π but 4π .

3. Time-reversal symmetry

The system has time-reversal symmetry,

$$H(\mathbf{k}) = \hat{\Theta}H(-\mathbf{k})\hat{\Theta}^{-1}, \quad (\text{B10})$$

$$\hat{\Theta}c_n(\mathbf{k})\hat{\Theta}^{-1} = \Theta c_n(-\mathbf{k}), \quad (\text{B11})$$

$$\hat{\Theta}c_n^{\dagger}(\mathbf{k})\hat{\Theta}^{-1} = c_n^{\dagger}(-\mathbf{k})\Theta^{-1}, \quad (\text{B12})$$

with $\Theta = -is_y\mathcal{K}$. Matrices $\epsilon(\mathbf{k})$ and t_z has the following relation,

$$\Theta\epsilon(\mathbf{k})\Theta^{-1} = \epsilon(-\mathbf{k}), \quad \Theta t_z \Theta^{-1} = t_z. \quad (\text{B13})$$

The $\bar{\Gamma}$ and \bar{M} points are time-reversal invariant momenta (TRIM), but the \bar{X} point is not. At \bar{X} : $(\pi, \pi) = \mathbf{G}_1/2$ and \bar{Y} : $(-\pi, \pi) = \mathbf{G}_2/2$ points, the different time-reversal symmetry is satisfied as

$$H(\mathbf{k} + \mathbf{G}_i/2) = \hat{\Theta}_{\bar{X}}H(-\mathbf{k} + \mathbf{G}_i/2)\hat{\Theta}_{\bar{X}}^{-1}, \quad (\text{B14})$$

with $\hat{\Theta}_{\bar{X}} = \mathcal{U}\hat{\Theta}$. Similarly to the periodicity in the previous section, the negative sign factor changes the symmetry in each mirror sector. $\hat{\Theta}_{\bar{X}}$ (anti)commutes with \mathcal{M} for odd (even) numbers of layers;

$$\mathcal{M}\hat{\Theta}_{\bar{X}} + (-1)^{N_z}\hat{\Theta}_{\bar{X}}\mathcal{M} = 0, \quad (\text{B15})$$

i.e., the system belongs to the class AII- U^+ in Ref. 71 (or AII- R_- in Refs. 69 and 70) in odd numbers of layers and to the class AII- U^- (or AII- R_+) in even numbers of layers. As a result, in the even numbers of layers, $\hat{\Theta}_{\bar{X}}$ symmetry requires Kramers pairs only at the \bar{X} and \bar{Y} points within each mirror sector. Note that Θ interchanges the mirror sectors; $\hat{\Theta}H_{\pm}(\mathbf{k})\hat{\Theta}^{-1} = H_{\mp}(-\mathbf{k})$, due to $[\hat{\Theta}, \mathcal{M}] = 0$.

4. Spatial-inversion symmetry

As in the case of the time-reversal symmetry, spatial-inversion symmetry takes different forms depending on the TRIM. At the $\bar{\Gamma}$ point, the inversion symmetry is expressed as follows,

$$H(\mathbf{k}) = \mathcal{P}H(-\mathbf{k})\mathcal{P}^{\dagger}, \quad (\text{B16})$$

$$\mathcal{P}c_n(\mathbf{k})\mathcal{P}^{\dagger} = \mathcal{P}c_{N_z+1-n}(-\mathbf{k}), \quad (\text{B17})$$

where \mathcal{P} acts on the orbital space. \mathcal{P} commutes with \mathcal{M} for both even and odd numbers of layers. On the other hand, at the \bar{X} point,

$$H(\mathbf{k} + \mathbf{G}_i/2) = \mathcal{P}_{\bar{X}}H(-\mathbf{k} + \mathbf{G}_i/2)\mathcal{P}_{\bar{X}}^{\dagger}, \quad (\text{B18})$$

with $\mathcal{P}_{\bar{X}} = \mathcal{U}\mathcal{P}$. $\mathcal{P}_{\bar{X}}$ (anti)commutes with \mathcal{M} for the odd (even) numbers of layers;

$$\mathcal{M}\mathcal{P}_{\bar{X}} + (-1)^{N_z}\mathcal{P}_{\bar{X}}\mathcal{M} = 0. \quad (\text{B19})$$

Equations (B15) and (B19) lead to

$$\mathcal{P}\hat{\Theta}H_{\pm}\Theta^{-1}\mathcal{P}^{\dagger} = H_{\mp}, \quad \mathcal{P}_{\bar{X}}\hat{\Theta}_{\bar{X}}H_{\pm}\Theta_{\bar{X}}^{-1}\mathcal{P}_{\bar{X}}^{\dagger} = H_{\mp}, \quad (\text{B20})$$

namely, all the energy bands in each sector is not doubly degenerated, except for the \bar{X} points.

5. Rotational symmetry

The film has C_4 symmetry along the z -axis:

$$H(\mathbf{k}) = C_4H(\mathbf{k}')C_4^{\dagger}, \quad C_4c_n(\mathbf{k})C_4^{\dagger} = C_4c_n(\mathbf{k}') \quad (\text{B21})$$

with $C_4 = e^{-ij_z\pi/2}$, where \mathbf{k}' is the rotated momentum and j_z denotes the z -component of the total angular momentum. Combination of C_4 , Θ , and \mathcal{U} leads to

$$H(\mathbf{k} + \bar{M}) = \tilde{C}_4H(-\mathbf{k}' + \bar{M})\tilde{C}_4^{\dagger}, \quad (\text{B22})$$

with $\tilde{\mathcal{C}}_4 = \mathcal{C}_4 \mathcal{U} \hat{\Theta}$ and $\bar{\mathbf{M}} = (\mathbf{G}_1 + \mathbf{G}_2)/2$ being the $\bar{\mathbf{M}}$ point. Furthermore, $\tilde{\mathcal{C}}_4$ (anti)commutes with \mathcal{M} for odd (even) numbers of layers;

$$\mathcal{M} \tilde{\mathcal{C}}_4 + (-1)^{N_z} \tilde{\mathcal{C}}_4 \mathcal{M} = 0. \quad (\text{B23})$$

From these relations and $\tilde{\mathcal{C}}_4^2 = -\mathcal{C}_4^2$, there are Kramers pairs if the states have the real eigenvalue (± 1) of \mathcal{C}_4 , for the even numbers of layers in each mirror sector.

Appendix C: Topological number in the even numbers of layers

The topological number ζ_{M} Eq. (11) is a \mathbb{Z} topological invariant protected by translational, reflection, and time-reversal symmetries. Definition and numerics for ζ_{M} are shown based on Refs. 72 and 73.

The (001)–films with odd numbers of layers has (001)–reflection symmetry. This allows us to define the mirror Chern number since time-reversal symmetry is broken within each mirror sector. Such a symmetry is called R_- in Refs. 69 and 70. The films with even numbers of layers, on the other hand, does not have (001)–reflection symmetry itself but they have the corresponding glide symmetry. It is possible to decompose the Hamiltonian of the even numbers of layers into two independent sectors in the same way as in the odd numbers of layers (Appendix B 1). But the mirror Chern number in the even numbers of layers always vanishes since time-reversal symmetry arises within each mirror sector (Appendix B 3). This symmetry is called R_+ . For class AII- R_+ in two spatial dimensions, the possible topological invariant is the \mathbb{Z}_2 number, which is the same as that in two-dimensional TI with time-reversal symmetry.^{69,70} However, this is not the case for the present problem since the Brillouin zone in each mirror sector is doubled (Appendix B 2) and time-reversal invariant momenta are located only at the $\bar{\text{X}}$ points, which are inner points in the doubled Brillouin zone, not at the zone center $\bar{\Gamma}$ point. This type of time-reversal symmetry stemming from glide symmetry is different from that in other systems: time-reversal invariant momenta are located at the zone center and boundary in conventional cases. Thus the \mathbb{Z}_2 invariant does not work in the even numbers of layers. Therefore, we introduce another topological invariant consistent with glide and time-reversal symmetries in two spatial dimension, as follows.

1. Definition

Each mirror sector for the even numbers of layers have the doubled periodicity Eq. (B9) in the momentum space. The Brillouin zone is also doubled ($-\pi \leq k_x, k_y \leq 2\pi$) as denoted by the solid lines in Fig. 16. We define a topological number $\zeta_{\text{M}} = (\zeta_+ - \zeta_-)/2$ in the even numbers of layers in the doubled Brillouin zone, where ζ_{\pm}

is defined by the winding number of the Wannier center;

$$\zeta_{\pm} = \frac{1}{2\pi} \int_0^{2\pi} dk_y \frac{\partial \theta_{\pm}(k_y)}{\partial k_y} - \frac{\theta_{\pm}(2\pi) - \theta_{\pm}(0)}{2\pi} \in \mathbb{Z}. \quad (\text{C1})$$

The Wannier center θ_{\pm} is obtained from the Wilson loop as

$$\theta_{\pm}(k_y) = \text{Im} \ln \det D_{\pm}(k_y) = \text{Im} \text{Tr} \ln D_{\pm}(k_y), \quad (\text{C2})$$

with

$$D_{\pm}(k_y) = \text{P exp} \left[i \int_{-\pi}^{\pi} dk_x A_{\pm}(\mathbf{k}) \right] B_{\pm}(k_y). \quad (\text{C3})$$

The non-Abelian Berry connection $A_{\pm}(\mathbf{k})$ and matrix $B_{\pm}(k_y)$ are given by

$$A_{\pm}(\mathbf{k}) = -i V_{\pm}^{\dagger}(k_x, k_y) \frac{\partial V_{\pm}(k_x, k_y)}{\partial k_x}, \quad (\text{C4})$$

and

$$B_{\pm}(k_y) = V_{\pm}^{\dagger}(\pi, k_y) V_{\pm}(-\pi, k_y), \quad (\text{C5})$$

where matrix $V_{\pm}(k_x, k_y)$ is defined by

$$V_{\pm}(k_x, k_y) = \left(|k_x, k_y, 1, \pm\rangle, \dots, |k_x, k_y, 2N_{\pm}, \pm\rangle \right), \quad (\text{C6})$$

with $|k_x, k_y, m, \pm\rangle$, $m = 1, \dots, 2N_{\pm}$, an eigenvector of the Hamiltonian for occupied states. Here m is an occupied band index in each mirror sector, and N_{\pm} is the number of the occupied states.

For numerical calculation, the following discretized form is useful,

$$\theta_{\pm}(k_y) = \sum_{i=0}^{N_x-1} \text{Im} \ln \det F_{i,i+1,\pm}(k_y) + \text{Im} \ln \det B_{\pm}(k_y), \quad (\text{C7})$$

where

$$F_{i,i+1,\pm}(k_y) = V_{\pm}^{\dagger}(k_i, k_y) V_{\pm}(k_{i+1}, k_y), \quad (\text{C8})$$

with $k_i = -\pi + 2\pi i/N_x$ and $i = 0, \dots, N_x$. Note that, in the numerical calculation, the following must be explicitly taken into account to preserve gauge symmetry. $V_{\pm}^{\dagger}(k_{i+1}, k_y)$ in $F_{i,i+1,\pm}(k_y)$ is the hermitian conjugate of $V_{\pm}(k_{i+1}, k_y)$ in $F_{i,i+1,\pm}(k_y)$. Similarly, $V_{\pm}^{\dagger}(\pi, k_y)$ and $V_{\pm}(-\pi, k_y)$ in $B_{\pm}(k_y)$ are the hermitian conjugates of $V_{\pm}(\pi, k_y)$ in $F_{N_x-1, N_x}(k_y)$ and $V_{\pm}^{\dagger}(-\pi, k_y)$ in $F_{0,1,\pm}(k_y)$, respectively.

The glide-winding number ζ_{M} can be extended to three-dimensional systems. If a system has glide symmetry as $H(k_x, k_y, 0) = M_0 H(k_x, k_y, 0) M_0^{\dagger}$ and $H(k_x, k_y, \pi) = M_{\pi} H(k_x, k_y, \pi) M_{\pi}^{\dagger}$ ($M_0 \neq M_{\pi}$ in general), a set of glide-winding numbers $\zeta_{\text{M}}|_{k_z=0}$ and $\zeta_{\text{M}}|_{k_z=\pi}$ at the symmetric planes of $k_z = 0$ and $k_z = \pi$ are the $\mathbb{Z} \times \mathbb{Z}$ invariant in three spatial dimension.

2. Symmetry

Quantity related to physical phenomena must be gauge invariant. Here we show the topological number ζ_{\pm} is invariant under $U(2N_{\pm})$ -gauge transformation. Furthermore, we explain that this number is quantized to an integer protected by spatial inversion symmetry.

a. Gauge symmetry

$\theta_{\pm}(k_y)$ is $U(2N_{\pm})$ -gauge invariant, as shown below. For $V_{\pm}(k_x, k_y) \rightarrow V_{\pm}(k_x, k_y)w_{\pm}(\mathbf{k})$, with $w_{\pm}(\mathbf{k}) \in U(2N_{\pm})$, the non-Abelian Berry connection is transformed to

$$A_{\pm}(\mathbf{k}) \rightarrow w_{\pm}^{\dagger}(\mathbf{k})A_{\pm}(\mathbf{k})w_{\pm}(\mathbf{k}) - iw_{\pm}^{\dagger}(\mathbf{k})\frac{\partial w_{\pm}(\mathbf{k})}{\partial k_x}, \quad (\text{C9})$$

and its integral of $U(1)$ part is given by

$$\begin{aligned} & \int_{-\pi}^{\pi} dk_x \text{Tr} A_{\pm}(\mathbf{k}) \\ & \rightarrow \int_{-\pi}^{\pi} dk_x \text{Tr} A_{\pm}(\mathbf{k}) - i \int_{-\pi}^{\pi} dk_x \frac{\partial}{\partial k_x} \text{Tr} \ln w_{\pm}(\mathbf{k}) \\ & = \int_{-\pi}^{\pi} dk_x \text{Tr} A_{\pm}(\mathbf{k}) \\ & \quad - i \text{Tr} \ln w_{\pm}(\pi, k_y) + i \text{Tr} \ln w_{\pm}(-\pi, k_y), \end{aligned} \quad (\text{C10})$$

And also, matrix $B_{\pm}(k_y)$ is transformed to

$$\begin{aligned} \text{Tr} \ln B_{\pm}(k_y) & \rightarrow \text{Tr} \ln B_{\pm}(k_y) \\ & \quad - \text{Tr} \ln w_{\pm}(\pi, k_y) + \text{Tr} \ln w_{\pm}(-\pi, k_y). \end{aligned} \quad (\text{C11})$$

These relations proves that the Wannier center $\theta_{\pm}(k_y)$ is gauge invariant.

b. Inversion symmetry

Inversion symmetry is preserved in both the even and odd numbers of layers (see Appendix B 4), i.e., inversion operator \mathcal{P} can be restricted onto the space spanned by the $2N_{\pm}$ occupied states; $\mathcal{P} \rightarrow \mathcal{P}_{\pm} \equiv P_{\pm} \mathcal{P} P_{\pm} \in U(2N_{\pm})$. The eigenvectors are transformed to

$$V_{\pm}(k_x, k_y) \rightarrow V_{\pm}(-k_x, -k_y)\mathcal{P}_{\pm}. \quad (\text{C12})$$

Therefore, one obtains

$$A_{\pm}(\mathbf{k}) = -\mathcal{P}_{\pm}^{\dagger} A_{\pm}(-\mathbf{k}) \mathcal{P}_{\pm}, \quad (\text{C13})$$

$$B_{\pm}(k_y) = \mathcal{P}_{\pm}^{\dagger} B_{\pm}(-k_y) \mathcal{P}_{\pm}, \quad (\text{C14})$$

namely the Wannier center satisfies the following relation,

$$\theta_{\pm}(k_y) = -\theta_{\pm}(-k_y). \quad (\text{C15})$$

This means that a winding number defined in the entire Brillouin zone ($-2\pi < k_y < 2\pi$, region I \cup II in Fig. 16) is twice as large as that in half the Brillouin zone ($0 < k_y < 2\pi$, region I in Fig. 16). This is why the topological number ζ_{\pm} is defined in $0 < k_y < 2\pi$ in Eq. (11). Moreover, at the spatial-inversion invariant momenta $k_y = 0$ and $k_y = 2\pi$, the Wannier center is fixed to $\theta_{\pm}(0), \theta_{\pm}(2\pi) = 0$ or π , which removes $2n\pi$ -ambiguity in the winding number. As a result, the winding number ζ_{\pm} is proven to be a \mathbb{Z} topological invariant.

c. Time-reversal symmetry

Time-reversal symmetry Eq. (B10) is preserved in the system but not in each mirror sector: $\hat{\Theta}$ interchanges the mirror-even and mirror-odd sectors as

$$A_{\pm}(\mathbf{k}) = \mathcal{T} A_{\mp}^*(-\mathbf{k}) \mathcal{T}^{-1}, \quad (\text{C16})$$

$$B_{\pm}(k_y) = \mathcal{T} B_{\mp}^T(-k_y) \mathcal{T}^{-1}, \quad (\text{C17})$$

with \mathcal{T} being a skew matrix. As a result, the Wilson loop satisfies

$$D_{\pm}(k_y) = \mathcal{T} D_{\mp}^T(-k_y) \mathcal{T}^{-1}. \quad (\text{C18})$$

which implies that the Wannier centers in each mirror sector are not independent,

$$\theta_{\pm}(k_y) = \theta_{\mp}(-k_y). \quad (\text{C19})$$

Equations (C15) and (C19) result in $\zeta_{+} + \zeta_{-} = 0$. Only the difference $\zeta_M = (\zeta_{+} - \zeta_{-})/2$ can take a finite value.

The even numbers of layers have the additional time-reversal symmetry at the \bar{X} point (see Appendix B 3). The non-Abelian Berry connection around the \bar{X} point ($= \mathbf{G}_i/2$) is transformed as

$$A_{\pm}(\mathbf{k} + \mathbf{G}_i/2) = \mathcal{T}_{\bar{X}} A_{\pm}^*(-\mathbf{k} + \mathbf{G}_i/2) \mathcal{T}_{\bar{X}}^{-1}. \quad (\text{C20})$$

Suppose the Wilson loop $D'_{\pm}(k_y)$ defined in region I [Fig. 16(a)] as

$$D'_{\pm}(k_y) = \text{P exp} \left[i \int_{-2\pi}^{2\pi} dk_x A_{\pm}(\mathbf{k}) \right], \quad (\text{C21})$$

where $V_{\pm}(2\pi, k_y) = V_{\pm}(-2\pi, k_y)$ is fixed due to Eq. (B9) $H_{\pm}(\mathbf{k}) = H_{\pm}(\mathbf{k} + \mathbf{G}_1 + \mathbf{G}_2)$. The Wannier center $\theta'_{\pm}(k_y) = \text{Im} \ln \det D'_{\pm}(k_y)$ satisfies the following relation,

$$\theta'_{\pm}(k_y + \pi) = \theta'_{\pm}(-k_y + \pi), \quad (\text{C22})$$

since $D'_{\pm}(k_y + \pi) = \mathcal{T}_{\bar{X}} D'_{\pm}^T(-k_y + \pi) \mathcal{T}_{\bar{X}}^{-1}$. Namely, a topological number defined in entire region I ($-2\pi \leq k_x \leq 2\pi, 0 \leq k_y \leq 2\pi$) in Fig. 16(a) vanishes. In order to extract nontrivial contribution of topological number, the domain is divided so that one half of Kramers pair is picked up. There are two ways to divide region I. One is $I \rightarrow \text{III} + \text{IV}$ [Fig. 16(b)]. That defined in region

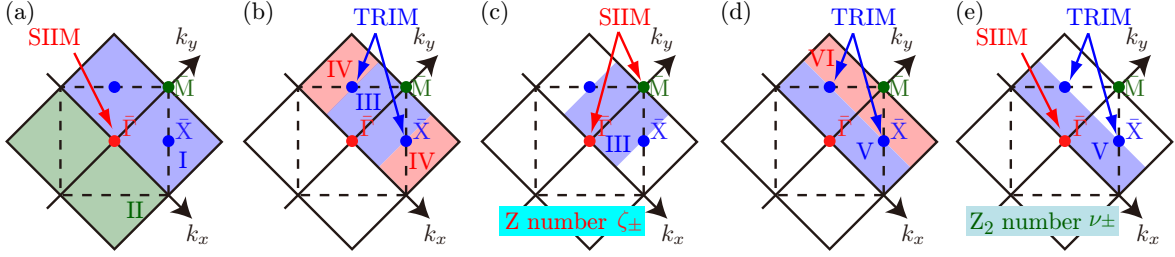


FIG. 16. Domain of integration for topological numbers. The dashed and solid lines indicate the projected Brillouin zone and that in each mirror sector for the even numbers of layers, respectively. The $\bar{\Gamma}$ ($k_x = 0, k_y = 0$) and \bar{M} ($2\pi, 0$) points are spatial-inversion invariant momenta (SIIM) and the \bar{X} point (π, π) is a time-reversal invariant momentum (TRIM). Regions I–VI denote the domain reduced by symmetries. Topological numbers defined in regions III and V are \mathbb{Z} (ζ_{\pm}) and \mathbb{Z}_2 (ν_{\pm}) numbers, respectively.

III [Fig. 16(c)] is the \mathbb{Z} topological invariant, which is already introduced in Eq. (C1). The other is $I \rightarrow V + VI$ [Fig. 16(d)]. A topological number ν_{\pm} defined in region V [Fig. 16(e)],

$$\nu_{\pm} = \int_0^{\pi} \frac{dk_y}{2\pi} \frac{\partial \theta'_{\pm}(k_y)}{\partial k_y} - \frac{\theta'_{\pm}(\pi) - \theta'_{\pm}(0)}{2\pi}, \quad (C23)$$

is a \mathbb{Z}_2 topological invariant, since eigenvalues of $D'_{\pm}(\pi)$ are doubly degenerated due to $\mathcal{T}_{\bar{X}} = -\mathcal{T}_{\bar{X}}^T$. The two-fold degeneracy leads to $4n\pi$ (not $2n\pi$) phase ambiguity in $\theta'(\pi)$. The spatial inversion symmetry requires $\theta'(0) = 0$, as in Eq. (C15). In consequence, $\nu_{\pm} \bmod 2$ is a \mathbb{Z}_2 topological invariant. In the actual calculation, however, $\nu_{\pm} = 0 \bmod 2$ is obtained. A nontrivial topological number in the even numbers of layers comes from ζ_M , which is explained in the following section.

3. Wannier-center flow

Here we show examples of the Wannier-center flow and the corresponding topological number ζ_M denoted in Fig.

10(a). Figure 17 shows the Wannier-center flow around the transition from $\zeta_M = 0$ to $|\zeta_M| = 2$. For $N_z = 12$, the Wannier center θ_+ in the mirror-even sector does not wind [Figs. 17(a) and 17(b)]. For $N_z = 14$, on the other hand, the Wannier center goes through the branch cut ($\theta = \pm\pi$) twice at $k \sim 0.914\pi$ and $k \sim 0.933\pi$. This results in the winding number of θ_+ is two, i.e., the corresponding topological number is given by $|\zeta_M| = 2$.

Figure 18 shows the Wannier-center flow for $N_z = 38$ and $N_z = 40$, where the topological number changes from $|\zeta_M| = 2$ to $\zeta_M = 0$. For $N_z = 38$, the Wannier center goes through the branch cut at $k_y \sim 0.913\pi$ and $k_y \sim 1.045\pi$, i.e., the winding number is obtained to be $|\zeta_M| = 2$. On the other hand, for $N_z = 40$, the Wannier center goes through the branch cut from above at $k_y \sim 0.913\pi$, but from below at $k_y \sim 0.97\pi$. Hence the winding number vanishes; $\zeta_M = -1 + 1 = 0$ for $N_z = 40$.

¹ M. Z. Hasan and C. L. Kane, Rev. Mod. Phys. **82**, 3045 (2010).

² X.-L. Qi and S.-C. Zhang, Rev. Mod. Phys. **83**, 1057 (2011).

³ Y. Ando, J. Phys. Soc. Jpn. **82**, 102001 (2013).

⁴ L. Fu, Phys. Rev. Lett. **106**, 106802 (2011).

⁵ T. H. Hsieh, H. Lin, J. Liu, W. Duan, A. Bansil, and L. Fu, Nat. Commun. **3**, 982 (2012).

⁶ Y. Tanaka, Z. Ren, T. Sato, K. Nakayama, S. Souma, T. Takahashi, K. Segawa, and Y. Ando, Nat. Phys. **8**, 800 (2012).

⁷ S.-Y. Xu, C. Liu, N. Alidoust, M. Neupane, D. Qian, I. Belopolski, J. D. Denlinger, Y. J. Wang, H. Lin, L. A. Wray, G. Landolt, B. Slomski, J. H. Dil, A. Marcinkova, E. Morosan, Q. Gibson, R. Sankar, F. C. Chou, R. J. Cava, A. Bansil, and M. Z. Hasan, Nat. Commun. **3**, 1192 (2012).

⁸ P. Dziawa, B. J. Kowalski, K. Dybko, R. Buczko, A. Szcz-

bakow, M. Szot, E. Łusakowska, T. Balasubramanian, B. M. Wojek, M. H. Berntsen, O. Tjernberg, and T. Story, Nat. Mater. **11**, 1023 (2012).

⁹ B. M. Wojek, R. Buczko, S. Safaei, P. Dziawa, B. J. Kowalski, M. H. Berntsen, T. Balasubramanian, M. Leandersson, A. Szczerbakow, P. Kacman, T. Story, and O. Tjernberg, Phys. Rev. B **87**, 115106 (2013).

¹⁰ Y. Tanaka, T. Sato, K. Nakayama, S. Souma, T. Takahashi, Z. Ren, M. Novak, K. Segawa, and Y. Ando, Phys. Rev. B **87**, 155105 (2013).

¹¹ A. Gyenis, I. K. Drozdov, S. Nadj-Perge, O. B. Jeong, J. Seo, I. Pletikosić, T. Valla, G. D. Gu, and A. Yazdani, Phys. Rev. B **88**, 125414 (2013).

¹² Y. Okada, M. Serbyn, H. Lin, D. Walkup, W. Zhou, C. Dhital, M. Neupane, S. Xu, Y. J. Wang, R. Sankar, F. Chou, A. Bansil, M. Z. Hasan, S. D. Wilson, L. Fu, and V. Madhavan, Science **341**, 1496 (2013).

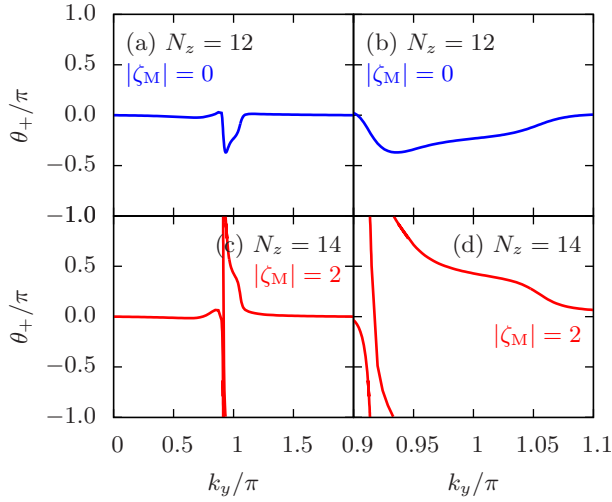


FIG. 17. Evolution of Wannier center in the mirror-even sector of SnTe films for $N_z = 12$ ($\zeta_M = 0$) [(a) and (b)] and $N_z = 14$ ($|\zeta_M| = 2$) [(c) and (d)].

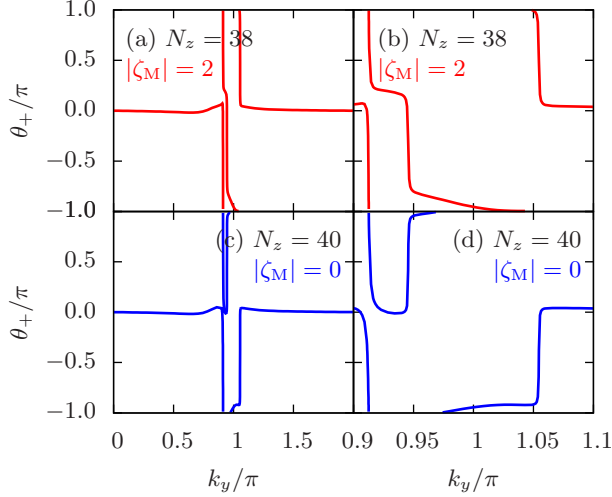


FIG. 18. Evolution of Wannier center in the mirror-even sector of SnTe films for $N_z = 38$ ($|\zeta_M| = 2$) [(a) and (b)] and $N_z = 40$ ($\zeta_M = 0$) [(c) and (d)].

- ¹³ S. Safaei, P. Kacman, and R. Buczko, Phys. Rev. B **88**, 045305 (2013).
- ¹⁴ R.-J. Slager, A. Mesaros, V. Jurićić, and J. Zaanen, Nat. Phys. **9**, 98 (2013), arXiv:1209.2610 [cond-mat.mes-hall].
- ¹⁵ M. Kargarian and G. A. Fiete, Phys. Rev. Lett. **110**, 156403 (2013).
- ¹⁶ Y. J. Wang, W.-F. Tsai, H. Lin, S.-Y. Xu, M. Neupane, M. Z. Hasan, and A. Bansil, Phys. Rev. B **87**, 235317 (2013).
- ¹⁷ M. Ye, J. W. Allen, and K. Sun, arXiv:1307.7191.
- ¹⁸ P. Barone, T. c. v. Rauch, D. Di Sante, J. Henk, I. Mertig, and S. Picozzi, Phys. Rev. B **88**, 045207 (2013).
- ¹⁹ C.-X. Liu and R.-X. Zhang, arXiv:1308.4717.
- ²⁰ H. Weng, J. Zhao, Z. Wang, Z. Fang, and X. Dai, arXiv:1308.5607.
- ²¹ Y. Sun, Z. Zhong, T. Shirakawa, C. Franchini, D. Li, Y. Li,

- S. Yunoki, and X.-Q. Chen, arXiv:1308.5657.
- ²² F. Zhang, X. Li, J. Feng, C. L. Kane, and E. J. Mele, arXiv:1309.7682.
- ²³ X.-J. Liu and K. T. Law, arXiv:1310.5685.
- ²⁴ T. Yokoyama, arXiv:1403.1962.
- ²⁵ A. S. Erickson, J.-H. Chu, M. F. Toney, T. H. Geballe, and I. R. Fisher, Phys. Rev. B **79**, 024520 (2009).
- ²⁶ S. Sasaki, Z. Ren, A. A. Taskin, K. Segawa, L. Fu, and Y. Ando, Phys. Rev. Lett. **109**, 217004 (2012).
- ²⁷ G. Balakrishnan, L. Bawden, S. Cavendish, and M. R. Lees, Phys. Rev. B **87**, 140507 (2013).
- ²⁸ R. D. Zhong, J. A. Schneeloch, X. Y. Shi, Z. J. Xu, C. Zhang, J. M. Tranquada, Q. Li, and G. D. Gu, Phys. Rev. B **88**, 020505 (2013).
- ²⁹ T. Sato, Y. Tanaka, K. Nakayama, S. Souma, T. Takahashi, S. Sasaki, Z. Ren, A. A. Taskin, K. Segawa, and Y. Ando, Phys. Rev. Lett. **110**, 206804 (2013).
- ³⁰ L. P. He, Z. Zhang, J. Pan, X. C. Hong, S. Y. Zhou, and S. Y. Li, Phys. Rev. B **88**, 014523 (2013).
- ³¹ P. Goswami and B. Roy, arXiv:1307.3240.
- ³² M. Novak, S. Sasaki, M. Kriener, K. Segawa, and Y. Ando, Phys. Rev. B **88**, 140502 (2013).
- ³³ D. J. Yu, F. Yang, L. Miao, C. Q. Han, M.-Y. Yao, F. Zhu, Y. R. Song, K. F. Zhang, J. F. Ge, X. Yao, Z. Q. Zou, Z. J. Li, B. Gao, D. D. Guan, C. Liu, C. L. Gao, D. Qian, and J.-f. Jia, arXiv:1402.4858.
- ³⁴ J. Linder, T. Yokoyama, and A. Sudbø, Phys. Rev. B **80**, 205401 (2009).
- ³⁵ H.-Z. Lu, W.-Y. Shan, W. Yao, Q. Niu, and S.-Q. Shen, Phys. Rev. B **81**, 115407 (2010).
- ³⁶ C.-X. Liu, H. Zhang, B. Yan, X.-L. Qi, T. Frauenheim, X. Dai, Z. Fang, and S.-C. Zhang, Phys. Rev. B **81**, 041307 (2010).
- ³⁷ W.-Y. Shan, H.-Z. Lu, and S.-Q. Shen, New J. Phys. **12**, 043048 (2010).
- ³⁸ K. Ebihara, K. Yada, A. Yamakage, and Y. Tanaka, Physica E **44**, 885 (2012).
- ³⁹ K.-I. Imura, M. Okamoto, Y. Yoshimura, Y. Takane, and T. Ohtsuki, Phys. Rev. B **86**, 245436 (2012).
- ⁴⁰ B. Singh, H. Lin, R. Prasad, and A. Bansil, Phys. Rev. B **88**, 195147 (2013).
- ⁴¹ M. Okamoto, Y. Takane, and K.-I. Imura, arXiv:1401.2583.
- ⁴² B.-J. Yang and N. Nagaosa, arXiv:1403.2207.
- ⁴³ Y. Sakamoto, T. Hirahara, H. Miyazaki, S.-i. Kimura, and S. Hasegawa, Phys. Rev. B **81**, 165432 (2010).
- ⁴⁴ Y. Zhang, K. He, Y. Zhang, K. He, C.-Z. Chang, C.-L. Song, L.-L. Wang, X. Chen, J.-F. Jia, Z. Fang, X. Dai, W.-Y. Shan, S.-Q. Shen, Q. Niu, X.-L. Qi, S.-C. Zhang, X.-C. Ma, and Q.-K. Xue, Nat. Phys. **6**, 584 (2010).
- ⁴⁵ A. A. Taskin, S. Sasaki, K. Segawa, and Y. Ando, Phys. Rev. Lett. **109**, 066803 (2012).
- ⁴⁶ A. A. Burkov and L. Balents, Phys. Rev. Lett. **107**, 127205 (2011).
- ⁴⁷ T. Fukui, K.-I. Imura, and Y. Hatsugai, J. Phys. Soc. Jpn. **82**, 073708 (2013).
- ⁴⁸ R. E. Simpson, P. Fons, A. V. Kolobov, T. Fukaya, M. Krbal, T. Yagi, and J. Tominaga, Nat. Nanotech. **6**, 501 (2011).
- ⁴⁹ J. Tominaga, R. E. Simpson, P. Fons, and A. V. Kolobov, Appl. Phys. Lett. **99**, 152105 (2011).
- ⁵⁰ K. Nakayama, K. Eto, Y. Tanaka, T. Sato, S. Souma, T. Takahashi, K. Segawa, and Y. Ando, Phys. Rev. Lett. **109**, 236804 (2012).

- ⁵¹ H. Lin and S.-T. Yau, *Int. J. Mod. Phys. B* **27**, 1350107 (2013).
- ⁵² C. Fang, M. J. Gilbert, and B. A. Bernevig, *Phys. Rev. Lett.* **112**, 046801 (2014).
- ⁵³ J. Liu, T. H. Hsieh, P. Wei, W. Duan, J. Moodera, and L. Fu, *Nat. Mater.* **13**, 178 (2014).
- ⁵⁴ M. Ezawa, arXiv:1402.4297.
- ⁵⁵ G. Yang, J. Liu, L. Fu, W. Duan, and C.-X. Liu, *Phys. Rev. B* **89**, 085312 (2014).
- ⁵⁶ A. A. Taskin, S. Sasaki, K. Segawa, and Y. Ando, arXiv:1305.2470.
- ⁵⁷ C. Yan, J. Liu, Y. Zang, J. Wang, Z. Wang, P. Wang, Z.-D. Zhang, L. Wang, X. Ma, S. Ji, K. He, L. Fu, W. Duan, Q.-K. Xue, and X. Chen, arXiv:1402.0609.
- ⁵⁸ B. A. Assaf, F. Katmis, P. Wei, B. Satpati, Z. Zhang, S. P. Bennett, V. G. Harris, J. S. Moodera, and D. Heiman, arXiv:1403.1810.
- ⁵⁹ C. S. Lent, M. A. Bowen, J. D. Dow, R. S. Allgaier, O. F. Sankey, and E. S. Ho, *Superlattices Microstruct.* **2**, 491 (1986).
- ⁶⁰ T. Fukui, Y. Hatsugai, and H. Suzuki, *Journal of the Physical Society of Japan* **74**, 1674 (2005).
- ⁶¹ A. Umerski, *Phys. Rev. B* **55**, 5266 (1997).
- ⁶² M. V. Berry, *Proc. R. Soc. Lond.* **392**, pp. 45 (1984).
- ⁶³ F. Wilczek and A. Zee, *Phys. Rev. Lett.* **52**, 2111 (1984).
- ⁶⁴ A. M. Turner, Y. Zhang, and A. Vishwanath, *Phys. Rev. B* **82**, 241102 (2010).
- ⁶⁵ T. L. Hughes, E. Prodan, and B. A. Bernevig, *Phys. Rev. B* **83**, 245132 (2011).
- ⁶⁶ X.-L. Qi, T. L. Hughes, and S.-C. Zhang, *Phys. Rev. B* **78**, 195424 (2008).
- ⁶⁷ M. Saghir, M. R. Lees, S. J. York, and G. Balakrishnan, *Cryst. Growth Des.* **14**, 2009 (2014).
- ⁶⁸ M. Safdar, Q. Wang, M. Mirza, Z. Wang, and J. He, *Cryst. Growth Des.* **14**, 2502 (2014).
- ⁶⁹ C.-K. Chiu, H. Yao, and S. Ryu, *Phys. Rev. B* **88**, 075142 (2013).
- ⁷⁰ T. Morimoto and A. Furusaki, *Phys. Rev. B* **88**, 125129 (2013).
- ⁷¹ K. Shiozaki and M. Sato, arXiv:1403.3331.
- ⁷² R. Yu, X. L. Qi, A. Bernevig, Z. Fang, and X. Dai, *Phys. Rev. B* **84**, 075119 (2011).
- ⁷³ A. Alexandradinata, X. Dai, and B. A. Bernevig, arXiv:1208.4234.